Advanced Powder Materials 5 (2026) 100407

Contents lists available at ScienceDirect

Advanced Powder Materials

journal homepage: www.keaipublishing.com/en/journals/advanced-powder-materials

Asymmetrically Cu–O–Cu bridged dual-atom sites on bio-functionalized oxides for molecular nitrate upcycling

Yeryong Lee[a,1], Akash Prabhu Sundar Rajan[a,1], Jayaraman Theerthagiri[a,1], Anuj Kumar[b,1], Wanwisa Limphirat[c], Ahreum Min[a,*], Myong Yong Choi[a,d,**]

[a] Department of Chemistry (BK21 FOUR), Research Institute of Advanced Chemistry, Gyeongsang National University, Jinju, 52828, Republic of Korea
[b] Nano-Technology Research Laboratory, Department of Chemistry, GLA University, Mathura, Uttar Pradesh, 281406, India
[c] Beamline Division, Synchrotron Light Research Institute (SLRI), Nakhon Ratchasima, 30000, Thailand
[d] Core-Facility Center for Photochemistry & Nanomaterials, Gyeongsang National University, Jinju, 52828, Republic of Korea

ARTICLE INFO

Keywords:
CO_2 laser–irradiation method
Asymmetric Cu dual-atom sites
L-tryptophan-functionalized Fe_3O_4/α-Fe_2O_3
Proton-coupled multielectron nitrate reduction
Ammonia synthesis

ABSTRACT

The electrochemical nitrate reduction reaction (NO_3RR) is a promising strategy for decentralized ammonia (NH_3) production and environmental remediation under ambient conditions. However, achieving complete eight-electron/nine-proton ($8e^-/9H^+$) conversion of NO_3^- to NH_3 with high selectivity and efficiency remains challenging owing to sluggish NO_3^- activation and competing N–N coupling side reactions such as N_2, N_2O, and NO gas evolution. Herein, we report a rationally designed Cu dual-atom (DA) catalyst composed of asymmetrically coordinated Cu atomic pairs anchored on an L-tryptophan-functionalized Fe_3O_4/α-Fe_2O_3 heterostructure (Cu_2/try-FeO_x), synthesized via a CO_2 laser irradiation method involving multi-step continuous-wave exposure for interface engineering. The hybrid Cu_2/try-FeO_x support provides abundant N and O coordination sites and enhanced electron mobility, enabling spatially separated Cu atom by asymmetrically coordinated Cu–N/O dual sites exhibit synergistic electronic interactions, forming robust DA configurations. In situ and ex situ spectroelectrochemical analyses, supported by theoretical calculations, confirm a $*NO_3 \rightarrow *NO_2 \rightarrow *NO \rightarrow *NHO \rightarrow *NH_2O \rightarrow *NH_3 \rightarrow NH_3$ reaction pathway. At the optimal potential, the total Faradaic efficiency toward NH_3 and NO_2^- approaches ~95%, indicating effective suppression of competing H_2, N_2, and N_2O formation and confirming a highly selective $8e^-/9H^+$ NO_3RR mechanism. Notably, NO_3RR tests using Cu_2/try-FeO_X achieve a high NH_3 yield rate of 0.29 mmol h^{-1} cm^{-2} and a maximum Faradaic efficiency of 88.5% at −0.2 V vs. RHE. Furthermore, when integrated into a Zn–NO_3^- battery, the catalyst enables self-powered NO_3^- to NH_3 conversion with stable operation over 100 h. This study presents a rational approach that integrates DA site engineering catalyst design with bio-functional support design to regulate intermediate adsorption and electron transfer, thereby enhancing the activity and selectivity for self-powered molecular NO_3^- upcycling technologies.

1. Introduction

Ammonia (NH_3) is a vital chemical in modern society, and its sustainable production under ambient environments is essential for accomplishing a carbon-neutral environment. Traditionally, NH_3 is synthesized via the Haber–Bosch process—an energy-intensive method dependable for over 1%–2% of global energy consumption and substantial carbon dioxide (CO_2) emissions [1–5]. As a substitute to the Haber–Bosch method, the electrochemical nitrate reduction reaction (NO_3RR) offers a low-temperature, low-pressure strategy to simultaneously produce NH_3 and removal of NO_3^- pollutants, which are common in agricultural and industrial wastewater. This dual-function approach is particularly attractive for decentralized NH_3 synthesis powered by renewable electricity [6–8]. Despite its advantage, the NO_3RR remains kinetically complex and mechanistically challenging. The conversion of NO_3^- to NH_3 is an eight-electron, nine-proton

* Corresponding author.
** Corresponding author. Department of Chemistry (BK21 FOUR), Research Institute of Advanced Chemistry, Gyeongsang National University, Jinju, 52828, Republic of Korea.
E-mail addresses: armin@gnu.ac.kr (A. Min), mychoi@gnu.ac.kr (M.Y. Choi).
Peer review under the responsibility of Central South University.
[1] These authors contributed equally to this work.

https://doi.org/10.1016/j.apmate.2026.100407
Received 11 November 2025; Received in revised form 16 January 2026; Accepted 5 February 2026
Available online 16 February 2026

($8e^-/9H^+$) process involving multiple adsorbed intermediates (*NO_3, *NO_2, *NO, *NHOH, and *NH_2), resulting in sluggish kinetics and competitive side reactions such as H_2 and NO gas evolution. Efficient catalysis of this transformation requires highly active and selective catalytic centers capable of stabilizing and converting nitrogenous intermediates while suppressing parasitic side reactions [9,10].

Transition metal–based catalysts, particularly those derived from earth-abundant elements such as Fe [11], Co [12], Ni [13,14], Cu [15–17], and Bi [18] have attracted considerable attention for the electrochemical NO_3RR owing to their natural abundance and diverse redox properties. Among them, Cu exhibits a stronger affinity for NO_3^- and NO_2^- and a favorable *d*-band center for stabilizing key intermediates (*NO_2 and *NO). However, Cu-based catalysts, particularly at the atomic scale, are prone to surface aggregation and poor long-term stability during the NO_3RR [19–21]. To address these challenges, recent studies have increasingly focused on the development of dual-atom catalysts (DACs), which exploit synergistic interactions between neighboring metal atoms [22,23]. These interactions in DACs create unique geometric and electronic configurations that enhance the NO_3RR kinetics, modulate intermediate binding energies, and enable alternative reaction pathways not accessible to single-atom catalysts or nanoparticle-based electrocatalysts [24–29]. However, most existing studies have primarily concentrated on heterometallic Cu-based DACs (e.g., Cu–Fe, Cu–Ni, and Cu–Co), aiming to enhance NO_3^- adsorption and intermediate activation through elemental synergy [30–32]. These heteronuclear systems differ fundamentally from homonuclear Cu dual sites and therefore do not isolate the intrinsic effects of Cu–Cu interactions or tailored coordination environments on NO_3RR performance. In contrast, homonuclear Cu dual-atom (Cu-DA) configurations provide a distinctive platform to elucidate how Cu–Cu electronic coupling and geometric proximity govern key reaction steps. Such systems enable a more fundamental understanding of the structure–activity relationships underlying NO_3RR, offering valuable insights into catalyst design principles beyond heterometallic synergy [33–35].

In addition, designing the substrate for DACs plays a significant role in defining the coordination environment, electron density, and stability of the metal sites. Fe-based oxides are well known for their reversible redox reaction (Fe^{2+}/Fe^{3+}), surface oxygen vacancies, and structural robustness, enabling them to function as charge carriers and catalytic supports for the NO_3RR process [36,37]. In particular, heterostructure substrates composed of mixed-valence oxides, such as Fe_3O_4/α-Fe_2O_3, can facilitate rapid charge redistribution and interfacial electron transfer—both critical for multielectron electrocatalytic processes [38–40]. To further enhance dual-atom (DA) stabilization and dispersion, substrate surfaces functionalized with organic ligands such as L-tryptophan can serve as anchoring agents for metal ions. L-tryptophan is an amino acid–rich molecule whose N- and O-comprising functional moieties (e.g., –COOH, $–NH_2$, and indole) provide multiple coordination sites for metal ions and promote strong metal–ligand interactions [41,42]. These functionalities also improve the dispersion of active sites and modulate the local electronic structure around them, enabling efficient adsorption, activation, and hydrogenation of NO_3^- during the NO_3RR process. However, conventional approaches for synthesizing such materials often involve complex, high-temperature, and energy-intensive procedures [42,43].

Herein, we report a CO_2 laser–irradiation method involving multi-step continuous-wave exposure for interface engineering strategy to construct asymmetrically coordinated Cu-DA sites on an L-tryptophan-functionalized mixed-phase Fe_3O_4/α-Fe_2O_3 (Cu_2/try-FeO_x) heterostructure, where L-tryptophan serves as a N-rich anchoring molecule. The mixed-iron oxide (FeO_x) substrate provides a highly conductive, redox-active platform that enhances interfacial electron mobility, while the dual-phase oxide junction promotes efficient charge separation. XPS and XAS analyses confirm the introduction of L-tryptophan onto FeO_x, enabling Cu anchoring through N and O coordination, leading to the establishment of stable Cu_2–N/O configurations with spatial separation and electronic asymmetry. This architecture not only stabilizes the Cu-DA sites but also enhances NO_3^- adsorption and activation, particularly improving the $NO_3^- \rightarrow NO_2^-$ conversion step. In situ and ex situ spectroscopic analyses confirm an NO_3RR pathway consistent with the sequence $NO_3^- \rightarrow NO_2^- \rightarrow$ *$NH_2 \rightarrow NH_3$, following an $8e^-/9H^+$ mechanism with no detectable N_2 or N_2O byproducts, highlighting high selectivity toward the NO_2^--mediated pathway. Moreover, integration of the Cu_2/try-FeO_X catalyst into a Zn–NO_3^- battery platform demonstrates its capability for self-powered NO_3^- to NH_3 conversion, achieving high NH_3 yield and long-term durability under room temperature and atmospheric pressure. This study not only elucidates the mechanistic role of Cu-based DACs in the NO_3RR but also highlights the advantages of Fe-based heterostructures in stabilizing and activating dual-metal sites. By tailoring interfacial coordination between Cu–O–Cu bridged sites and the FeO_x substrate, along with modulating their local electronic environments, we propose a robust strategy for advancing the NO_3RR catalysis and decentralized NH_3 production technologies.

2. Results and discussion

2.1. Mechanistic analysis of structural evolution

The surface-functionalized, cubic-structured FeO_x was employed as a conductive and chemically active substrate for the subsequent loading of Cu-DA via a CO_2 laser–irradiation method involving multi-step continuous-wave exposure for interface engineering process, as shown in Fig. 1a. First, the cubic-structured Fe-based Prussian Blue Analogue (FePBA) was synthesized through a self-assembly co-precipitation method involving coordination between Fe^{2+} and $[Fe(CN)_6]^{3-}$, followed by recrystallization under solution supersaturation conditions (Fig. S1). The prepared FePBA contains Fe^{2+} and Fe^{3+} oxidation states, coordinated with C≡N bridges to form a three-dimensional (3D) porous framework. Upon thermal decomposition, FePBA is converted into a mixed-valence metal oxide, where Fe^{2+} and Fe^{3+} reorganize into a a heterostructure composed of Fe_3O_4/α-Fe_2O_3 (FeO_x) (Fig. 1a). This transformation is driven by the rapid decomposition of the cyanide-bridged Fe^{2+}/Fe^{3+} coordination framework under high-temperature conditions [44,45]. The phase evolution during this conversion was analyzed using XRD, as revealed in Fig. 1b. The initial FePBA framework exhibits characteristic peaks matching the crystal structure of $K_2Fe[Fe(CN)_6]$ (JCPDS No. 31–1000). After thermal treatment of FePBA framework, the XRD pattern displays distinct peaks corresponding to the Fe_3O_4 and α-Fe_2O_3 phases, indicating the formation of a heterojunction-interfaced oxide. Specifically, the FeO_X sample exhibits major diffraction peaks at 30.36° (220), 35.77° (311), 38.43° (220), 43.01° (422), 53.46° (511), and 57.39° (440), which are indexed to Fe_3O_4 (JCPDS No. 19-0629), and 23.27° (012), 33.10° (104), 40.85° (113), 49.61° (024), and 55.30° (116), which are indexed to α-Fe_2O_3 (JCPDS No. 33-0664) [46]. To further investigate the chemical evolution during this transformation, Raman (Fig. 1c) and Fourier transform infrared (FTIR) spectroscopy (Fig. 1d) were employed. In both the Raman and FTIR spectra, the FePBA sample exhibits a sharp vibrational peak at ~2100 cm^{-1}, accredited to the C≡N stretching mode of the cyanide bridging ligands. In the FeO_X sample, this nitrile group peak is completely absent, indicating the complete decomposition of the cyanide framework under thermal treatment, evolving into nitrogen and carbon monoxide gases. In addition, the Raman bands at 520.67 and 728.94 cm^{-1} in FePBA, attributed to metal–cyanide coordination within the PBA framework, are no longer present after its thermal treatment. Instead, new peaks appear at 214.0, 271.8, 374.1, 674.9, and 1284.3 cm^{-1}. corresponding to metal–oxygen lattice vibrations of the resulting FeO_x structures. These features confirm the successful formation of a dual-phase Fe_3O_4/α-Fe_2O_3 heterostructure, consistent with the XRD results [47,48].

Additionally, FESEM and HRTEM were conducted to reveal the surface morphology and heterojunction interface between Fe_3O_4 and

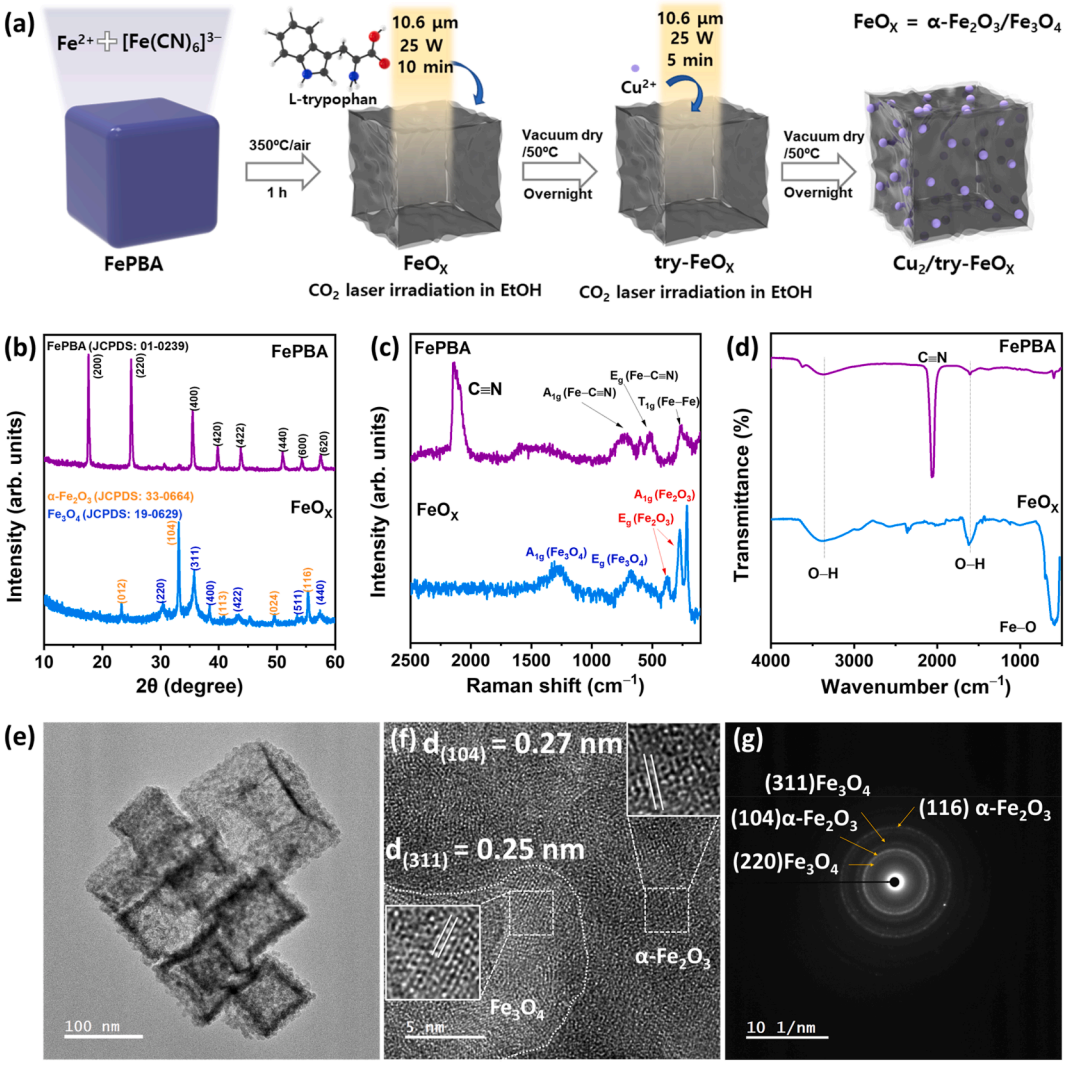

Fig. 1. (a) Schematic of the preparation of Cu_2/try-FeO_x via CO_2 laser–irradiation. (b–d) XRD, Raman, and FTIR spectra of FePBA and FeO_x. (e-f) TEM and HRTEM image showing lattice fringes of α-Fe_2O_3 ($d_{(104)}$=0.27 nm) and Fe_3O_4 ($d_{(311)}$=0.25 nm). (g) SAED pattern confirming the coexistence of α-Fe_2O_3:Fe_3O_4 through indexed diffraction rings.

α-Fe_2O_3 within the FeO_x substrate. The FESEM images (Fig. S2) reveal a well-defined 3D nanocube morphology that is retained in the FePBA and FeO_x materials. EDS elemental mapping reveals the presence of C, N, and Fe in FePBA, and primarily O and Fe in FeO_x, indicating the successful thermal conversion of FePBA to FeO_x while preserving the nanocube morphology. HRTEM images (Fig. 1e) show that the FeO_x structures consist of hollow nanocubes with an average size of ~200 nm. Further HRTEM analysis (Fig. 1f) reveals two distinct lattice fringes with spacings of 0.25 and 0.27 nm, consistent to the (311) plane of Fe_3O_4 and the (104) plane of α-Fe_2O_3, correspondingly. The close spatial proximity of these lattice planes confirms the formation of a crystallographically aligned Fe_3O_4/α-Fe_2O_3 heterojunction interface within FeO_x. The selected area electron diffraction pattern (Fig. 1g) displays well-defined diffraction rings that further support this structural assignment: Fe_3O_4 (311) plane and the α-Fe_2O_3 (104) phase [49,50]. These observations, including nanocube retention, lattice spacing, and elemental distribution are reliable with the XRD, Raman, and FTIR results, collectively validating the successful formation of a Fe_3O_4/α-Fe_2O_3 heterojunction through the thermal decomposition of FePBA.

XPS provides further insight into the surface composition and chemical states of the materials. The survey spectra confirm the presence of Fe, O, C, and N in FePBA, and primarily Fe and O in FeO_x (Fig. S3a). The C 1*s* spectrum of FePBA exhibits distinct signals at 284.2 and 287.9 eV, accredited to M−C and C≡N bonding, respectively. In FeO_x, the C≡N peak disappears, while the remaining carbon signals are attributed to adventitious carbon contamination (Fig. S3b). The N 1*s* region of FePBA shows a peak at 397.7 eV owing to the cyanide nitrogen, which is absent in FeO_X, indicating complete removal of C≡N ligands during thermal decomposition of FePBA (Fig. S3c). The O 1*s* spectrum of FeO_x displays a dominant peak at 539.9 eV, associated with lattice oxygen, along with a shoulder feature corresponding to surface oxygen species (Fig. S3d). Notably, the Fe 2*p* spectrum of FeO_x (Fig. S3e) shows coexisting Fe^{2+} and Fe^{3+} oxidation states with a systematic binding energy shift relative to FePBA; the Fe^{2+} $2p_{3/2}$ peak shifts by +1.05 eV and the Fe^{3+} $2p_{3/2}$ by +1.19 eV, indicating a change in the local electronic environment and increased electron delocalization at the Fe_3O_4/α-Fe_2O_3 interface (Fig. S3e). This positive shift in the Fe core-level binding energies suggests stronger Fe–O interactions in FeO_x compared to FePBA, indicating altered electron density at the interface region. Such electronic modulation of the substrate is beneficial for electrocatalytic applications. In particular, increased electron density at the heterojunction interface facilitates fast interfacial charge transfer and enhances coupling the electronic coupling between the FeO_x substrate and the DA active sites [51]. Furthermore, ultraviolet photoelectron spectroscopy (UPS) spectra of FeO_x and α-Fe_2O_3

(Fig. S4) reveals a reduced work function (12.15 eV) and a valence band edge in FeO_x positioned closer to the Fermi level, supporting the high electron mobility of the FeO_x substrate [52].

2.2. Immobilization of Cu-DA sites on the try-FeO_x substrate

To immobilize the Cu-DA on the FeO_xsubstrate surface, the FeO_X surface was first functionalized with L-tryptophan using CO_2 laser (λ=10.6 μm, 25 W) irradiation, yielding a functionalized material referred to as try-FeO_x. Based on our previous study [41], we propose that L-tryptophan binds to FeO_x through nucleophilic substitution and dehydration, in which a carboxyl linkage forms between the –C–OH group of L-tryptophan and terminal –OH groups on the FeO_x surface, as illustrated in Fig. S5. Subsequently, CO_2 laser–irradiation was applied again to induce Cu chelation onto the try-FeO_x surface, facilitating the formation of Cu-DA sites. The L-tryptophan on the FeO_x absorbs the localized laser generated–thermal energy, enhancing the molecular mobility and promoting interaction between Cu^{2+} and donor sites present in L-tryptophan and the FeO_X matrix. This process stabilizes Cu^{2+} through Cu–N and Cu–O coordination, resulting in the immobilization of atomically dispersed Cu species within the hybrid FeO_x framework, denoted as Cu_2/try-FeO_x [53]. Notably, the Cu loading in Cu_2/try-FeO_x is intrinsically constrained by the finite density of coordination sites provided by the L-tryptophan–functionalized FeO_x support. As a result, increasing the concentration of the Cu precursor does not lead to a measurable increase in Cu loading, confirming a coordination-site–limited stabilization mechanism. Covalent bonding and surface modification of FeO_x with L-tryptophan were confirmed via FTIR spectroscopy (Fig. 2a). In addition to the Fe–O vibrational peak at 591 cm^{-1}, new peaks corresponding to C–H stretching (852 and 1338 cm^{-1}) and C–O stretching (~1059 cm^{-1}) confirm the successful functionalization of L-tryptophan on the FeO_x surface. Upon Cu incorporation into try-FeO_X, the FTIR spectrum of resulting Cu_2/try-FeO_x exhibits a notable reduction in the intensities of organic vibrational bands, including those of C–H, C–O, and –OH signals, indicating changes in the molecular environment because of the direct coordination of Cu with O-containing functional groups on try-FeO_x [42,54]. Notably, Raman spectroscopy (Fig. S6) reveals no significant shifts in vibrational bands, indicating that the bulk structure of the FeO_x support remains considerably preserved upon Cu incorporation. Aberration-corrected HAADF--STEM imaging was performed to envision the atomic dispersion of Cu in the Cu_2/try-FeO_x composite (Fig. 2b). Elemental mapping (Fig. S7) confirms the uniform distribution of Cu throughout the FeO_x scaffold, colocalized with O and N. Compared with the try-FeO_x substrate, the Cu_2/try-FeO_x sample shows bright, discrete atomic features corresponding to isolated Cu atoms. Dual Cu atomic pairs (highlighted in the white rectangle) exhibit an average interatomic spacing of 3.03 Å (Fig. 2b). Furthermore, FESEM–EDS and inductively coupled plasma analyses indicate a total Cu loading of 4.63 wt%, uniformly distributed across the try-FeO_x surface (Fig. S8 and Table S1). These DA Cu configurations, with short interatomic spacings, are expected to promote synergistic electronic interactions and facilitate intermediate adsorption during the NO_3RR processes.

XPS analysis was performed to elucidate the surface chemical states and electronic configurations of try-FeO_x and Cu_2/try-FeO_x. The survey spectra (Fig. S9a) confirm the existence of Fe, O, C, and N in both samples, while Cu signals are observed exclusively in the Cu_2/try-FeO_x catalyst. As revealed in Fig. S9b, the high-resolution N 1*s* spectrum of try-FeO_x reveals signals attributed to N-containing groups from L-tryptophan, such as the amino group and indole nitrogen, confirming the successful functionalization of the FeO_x surface. The higher intensity of the amino-N peak compared to the indole-N peak is attributed to localized lone pair electrons on the amino group of L-tryptophan, which promote strong coordination with metal centers and enhance their stabilization on the substrate [55–57]. Upon Cu incorporation into try--FeO_x, the resulting Cu_2/try-FeO_x exhibits a new peak in the N 1*s* region consistent to metal–nitrogen (M−N) bonding, indicating coordination between Cu atoms and the amino nitrogen groups of L-tryptophan. This observation supports the hypothesis that N-based coordination plays a critical role in stabilizing Cu atoms on the try-FeO_x surface. The O 1*s* spectra (Fig. S9c) were deconvoluted into components corresponding to the metal–oxygen bonds (Fe–O), surface hydroxyl groups (–OH), and adsorbed H_2O. The binding energies and relative intensities of these chemical states remain largely unchanged between try-FeO_x and Cu_2/try-FeO_x, suggesting that the surface oxygen species are preserved upon Cu incorporation into try-FeO_x. Similarly, the C 1*s* spectra (Fig. S9d) of try-FeO_x show peaks consistent to C–C, C–N/C=C, and C=O species characteristic of L-tryptophan; these signals are retained in Cu_2/try-FeO_x, indicating that Cu coordination does not disrupt the organic moieties contributed by L-tryptophan on the FeO_x surface. The Fe 2*p* spectra (Fig. S9e) display characteristic multiplet splitting associated with Fe^{3+} and Fe^{2+} oxidation states in both samples, confirming the structural preservation of the FeO_x matrix. However, in Cu_2/try--FeO_x, the Fe 2*p* signals display a slight shift toward higher binding energies compared to FeO_x, suggesting a reduced electron density at the Fe centers. This shift is attributed to interfacial charge transfer from Fe centers to the adjacent Cu atoms at the Cu_2/try-FeO_x interface, as well as the electronic influence of L-tryptophan-derived surface functionalities, which collectively modulate the local electronic structure around Fe [58]. To investigate the atomically dispersed Cu species in Cu_2/try-FeO_x, high-resolution XPS analysis of the Cu 2*p* region was conducted (Fig. 2c). The Cu 2*p* spectrum displays signals at 932.9 and 934.6 eV, consistent to Cu^+ and Cu^{2+} oxidation states, respectively. These findings confirm that Cu atoms are stabilized via coordination with both nitrogen sites from L-tryptophan and oxygen terminations on the FeO_x surface, indicating a synergistic Cu–N–(tryptophan) and Cu–O–(FeO_x) interaction. This dual coordination environment supports the atomic dispersion and stabilization of Cu species in Cu_2/try-FeO_x.

To further evaluate the coordination environment and chemical state in Cu_2/try-FeO_x, XANES and EXFAS analyses were done using standard reference materials. These measurements were performed at the Core-Facility Center for Photochemistry & Nanomaterials, Gyeongsang National University, using the in situ cryo X-ray absorption spectrometer, IC-XAS (NFEC-2025-07-307201). As shown in the Cu *K*-edge XANES spectrum (Fig. 2d), the absorption edge position of Cu_2/try-FeO_x lies between those of metallic Cu^0 and Cu^{2+} oxide reference materials. The inset of Fig. 2d indicates that the isolated Cu atoms exhibit an average oxidation state close to Cu^{2+}. This suggests partial charge transfer between the Cu sites and surrounding O/N ligands from try-FeO_x. Similarly, the Fe *K*-edge XANES spectrum (Fig. S10a) displays a white-line feature located between those of Fe_3O_4 and Fe_2O_3 reference materials. In addition, the existence of a pre-edge peak corresponding to the $1s \rightarrow 3d$ electronic transition (Fig. S10b) confirms the dominance of octahedrally coordinated Fe sites, particularly at the Fe_3O_4/α-Fe_2O_3 interface [59]. The intensity and position of this pre-edge feature reflect local structural reorganization due to interfacial phase integration and rearrangement between Fe_3O_4 and α-Fe_2O_3 domains, leading to altered Fe coordination environments and Fe–O bond characteristics that enhance charge transfer and intermediate binding during electrochemical reactions [60]. These findings are reliable with the XRD, Raman, and XPS analyses, which support the formation of the Fe_3O_4/α-Fe_2O_3 heterostructure. To quantitatively determine the composition of the mixed-phase FeO_x, linear combination fitting (LCF) of the Fe *K*-edge XANES spectrum was performed using Fe_2O_3 and Fe_3O_4 as reference materials (Fig. S11) [61]. The fitting results (Table S2; total weight sum = 1.000, indicating proper normalization based on the sum of fractional phase contributions) reveal Fe_2O_3 and Fe_3O_4 contributions of 50.1%±4.0% and 49.9%±4.0%, respectively, to the overall FeO_x composition. The low residual fitting error (R-factor=0.0108) confirms the robustness of the LCF model in accurately quantifying the relative phase composition of FeO_x and highlights the phase heterogeneity arising from the coexistence of Fe_2O_3 and Fe_3O_4 domains within the FeO_x material.

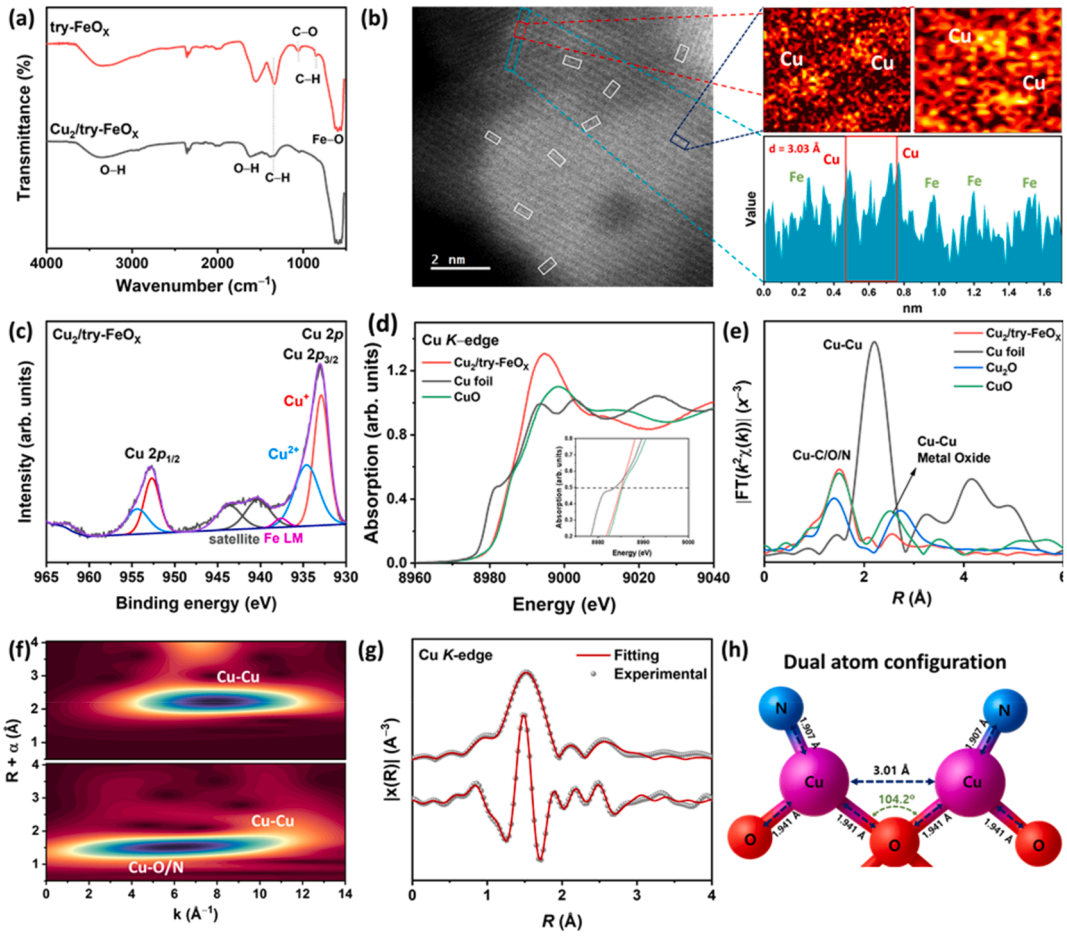

Fig. 2. (a) FTIR spectra of try-FeO_x and Cu_2/try-FeO_x. (b) HAADF-STEM image of Cu_2/try-FeO_x and corresponding magnified regions with intensity profile and interatomic spacing (d=3.03 Å). (c) Cu 2*p* XPS spectrum of Cu_2/try-FeO_x. (d–g) Cu *K*-edge XANES spectra, FT-EXAFS analysis in R space, WT-EXAFS contour plots with Cu foil reference, and FT-EXAFS fitting curves in both R and K space for Cu_2/try-FeO_x. (h) Schematic illustration of the predicted spatially separated Cu-DA configuration stabilized on the try-FeO_x support.

To understand the coordination structure of stabilized Cu-DA sites in the try-FeO_x catalyst, FT k^2-weighted EXFAS was performed, with reference spectra from the Cu foil, Cu_2O, and CuO shown in Fig. 2e. The first scattering peak in the EXFAS spectrum of Cu_2/try-FeO_x appears at ~1.50 Å, corresponding to the metal–ligand coordination environment. Based on previous analysis, this peak is attributed to a combination of Cu–N and Cu–O bonds in the Cu-DA sites. In addition, a broad feature centered at ~2.50 Å suggests the presence of two Cu centers spatially separated and bridged by oxygen atoms from the try-FeO_x lattice, rather than directly bonded. Notably, the absence of a Cu–Cu scattering peak at ~2.20 Å confirms the lack of metallic Cu–Cu bonding, further supporting the atomic dispersion of the Cu species. To gain further insight, wavelet transform (WT) study of the Cu *K*-edge EXAFS was conducted for Cu_2/try-FeO_x (Fig. 2f). The WT contour plot displays a prominent intensity maximum at ~4.5 $Å^{-1}$, consistent to the Cu–N coordination shell. A secondary feature at ~7.5 $Å^{-1}$, assigned to Cu–Cu scattering, appears with significantly low intensity, suggesting weak or less frequent Cu–Cu interactions. Importantly, the shift in the WT maxima for the Cu–Cu paths in Cu_2/try-FeO_x, relative to the Cu foil indicates a distinct local geometric and electronic environment around the Cu centers. Quantitative EXAFS fitting at the Cu *K*-edge enabled the precise determination of local coordination environments and interatomic distances around the Cu centers, providing detailed structural insights into the DA configuration (Fig. 2g–Table S3). The fitted bond lengths for Cu–O and Cu–N were estimated as 1.94 and 1.90 Å [62], respectively, with corresponding coordination numbers (CNs) of 2 and 1. Moreover, the two Cu atoms are separated by 3.01 Å, in good agreement with the DA configuration confirmed by EXFAS fitting (R-factor=0.00184), indicating an excellent quality of fit. The simultaneous presence of Cu–O, Cu–N, and Cu–Cu scattering paths within the same local coordination environment demonstrates that the Cu atoms are not isolated single sites but are spatially separated and structurally correlated. This coordination environment is consistent with an asymmetrically coordinated Cu–O–Cu DA motif, in which the two Cu centers are bridged by oxygen atoms associated with the FeO_x support while being simultaneously coordinated by nitrogen atoms from the L-tryptophan ligand (Fig. 2h) [42]. The successful formation of spatially separated Cu-DA sites in the try-FeO_x substrate is anticipated to synergistically enhance the NO_3RR performance of Cu_2/try-FeO_x by improving its intermediate binding and electron transfer capabilities.

2.3. Electrocatalytic NO_3RR performance

To elucidate the catalytic activity and selectivity of Cu_2/try-FeO_x for the NO_3RR, a comprehensive series of electrochemical measurements and NH_3 quantification experiments were conducted. Comparative studies were also performed using try-FeO_x and FePBA to assess the role of Cu-DA sites on the try-FeO_x surface. All electrochemical measurements were carried out in a three-electrode H-type cell, in which the anodic and cathodic compartments were separated by a Nafion membrane, as illustrated in Fig. S12a. All reported potentials are referenced to the reversible hydrogen electrode (RHE). As shown in Fig. 3a, the

electrochemical NO_3RR activity was initially evaluated using LSV in 1.0 M KOH, with and without 0.5 M KNO_3. The Cu_2/try-FeO_x catalyst exhibited a suggestively earlier onset potential and higher cathodic current density compared with FeO_x and FePBA. Specifically, Cu_2/try-FeO_x displayed an onset potential of −0.1 V vs. RHE, whereas FeO_x and FePBA showed NO_3^- reduction onset only beyond −0.2 V (Fig. S12). This improved onset potential indicates a low energy barrier for NO_3^- activation, likely owing to the electron-rich coordination environment around the Cu centers in Cu_2/try-FeO_x. Moreover, the LSV curves recorded in the absence of NO_3^- showed negligible current, confirming the minimal interference from the HER and highlighting the NO_3^- selective behavior of Cu_2/try-FeO_x. Supporting the LSV results, Tafel slope analysis, EIS, and electrochemical active site measurements (Figs. S13–S15) provided further insights into the electrocatalytic behavior of the Cu_2/try-FeO_x. The smallest Tafel slope observed for Cu_2/try-FeO_x in 1.0 M KOH (Fig. S13) reflects accelerated interfacial charge-transfer kinetics, suggesting that the reaction rate is governed by a proton-coupled electron transfer (PCET) step associated with the hydrogenation of the $*NO_2$ intermediate. EIS measurements revealed the lowest charge transfer resistance (R_{ct}) for Cu_2/try-FeO_x among all samples, with and without NO_3^-, indicating superior interfacial electron transport enabled by the Cu-DA sites. Furthermore, Cu_2/try-FeO_x possessed the highest active site density of 0.279 μmol cm^{-2}, followed by FeO_x (0.185 μmol cm^{-2}) and FePBA (0.109 μmol cm^{-2}). These findings highlight the synergistic effect between the try-FeO_x support and Cu atoms, enhancing NO_3^- adsorption and accelerating charge transfer at the Cu-DA active centers.

To further assess the NO_3RR efficiency, the NH_3 yield rate (YR) was determined at various applied potentials using the indophenol blue colorimetric process (Fig. S16). The ultraviolet–visible (UV–vis) absorbance of the catholyte was analyzed after 1 h of electrolysis at each potential to quantify NH_3 produced during the NO_3RR (Fig. S17 and **S18**). As revealed in Fig. 3b, Cu_2/try-FeO_x reaches a maximum NH_3 YR of 0.47 mmol h^{-1} cm^{-2} at −0.4 V vs. RHE. The sharp rise in YR between −0.1 and −0.2 V vs. RHE suggests the onset of rapid multielectron transfer, while the slight decline beyond −0.3 V indicates increasing competition from the HER at increasingly negative potentials. By contrast, FePBA and FeO_x exhibited maximum NH_3 YRs of only 0.21 and 0.31 mmol h^{-1} cm^{-2}, correspondingly. The Faradaic efficiency (FE) was concurrently evaluated (Fig. 3c), with Cu_2/try-FeO_X achieving a remarkable FE of 88.48% at −0.2 V vs. RHE, outperforming FeO_x (59.97%) and FePBA (41.84%). These results indicate that Cu-DA sites enhance NO_3^- adsorption, stabilize key intermediates, and facilitate their efficient conversion to NH_3. The consistently higher NH_3 YR and FE across the full potential range confirm the intrinsic electrocatalytic advantage of Cu_2/try-FeO_x.

The NO_3RR typically proceeds via a two-step mechanism: $NO_3^- \rightarrow NO_2^- \rightarrow NH_3$. Thus, NO_2^- is a key intermediate and a potential prematurely released byproduct during the NO_3RR process. To quantify NO_2^- alongside NH_3, a colorimetric method using the Griess reagent was employed (Fig. S19 and S20). As shown in Fig. S21, Cu_2/try-FeO_x exhibits a higher NO_2^- YR compared to FePBA and FeO_x, suggesting enhanced intermediate formation during the NO_3RR process. To confirm that NO_2^- is not a final product but an intermediate undergoing further reduction, electrolysis was extended to 10 h at a fixed potential (Fig. S22). The gradual decrease in the NO_2^- concentration, accompanied

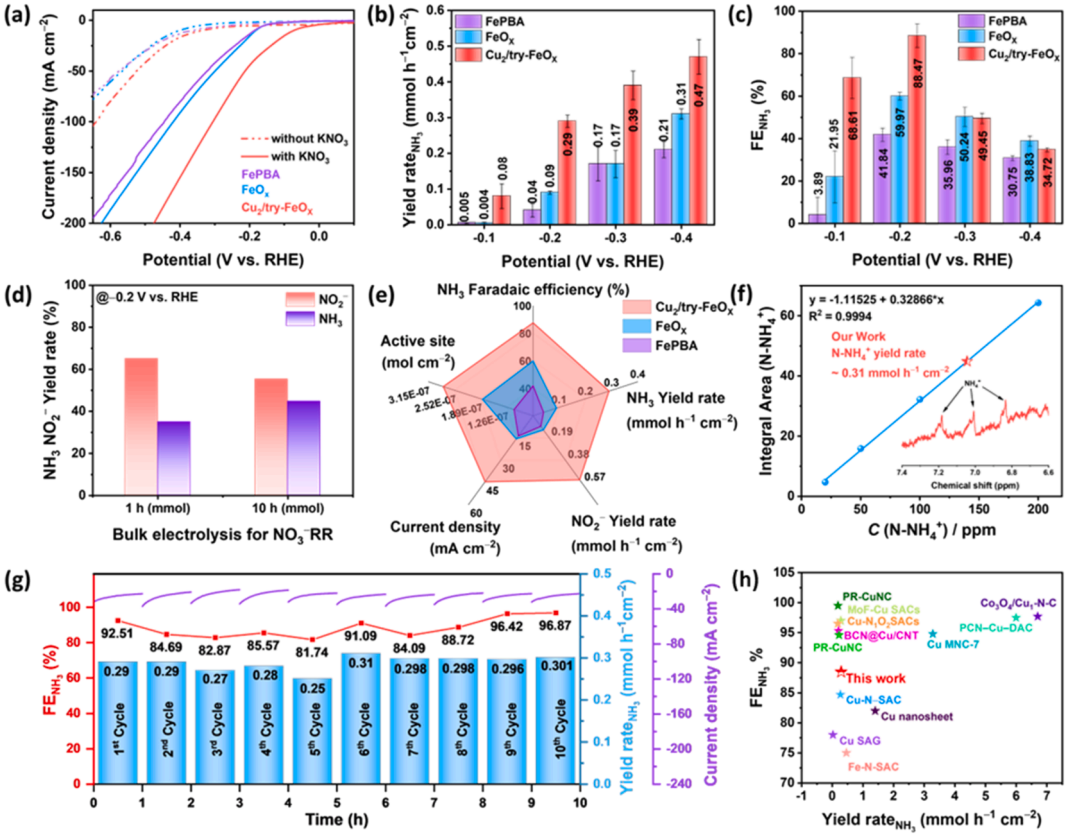

Fig. 3. (a) LSV curves of FePBA, FeO_x, and Cu_2/try-FeO_x in 1.0 M KOH with (solid line) and without 0.5 M KNO_3 (dash line. (b,c) NH_3 YR and FE during 1 h of the NO_3RR at different reduction potentials for FePBA, FeO_x, and Cu_2/try-FeO_x. (d) NO_2^- YRs during 1 h of the NO_3RR for FePBA, FeO_x, and Cu_2/try-FeO_x at different reduction potentials. (e) Comparative active site density, current density, NH_3 YR, FE, and NO_2^- YR for different catalysts during 1 h of the NO_3RR. (f) Linear calibration curve for NH_3 quantification from ^1H NMR integral peak area of known NH_4Cl concentrations and ^1H NMR spectra of catholyte collected after 1 h of the NO_3RR with Cu_2/try-FeO_x at −0.2 V vs. RHE. (g) Ten successive 1-h NO_3RR cycles with NH_3 YR and FE for Cu_2/try-FeO_x at −0.2 V vs. RHE, replenishing fresh catholyte each cycle. (h) Comparative NH_3 YR and FE graph with recently reported Cu-based electrocatalysts.

by a continuous increase in the NH_3 YR (Fig. 3d), supports efficient time-dependent conversion of NO_2^- into NH_3. This time-dependent behavior highlights the ability of the catalyst to facilitate the full $8e^-/9H^+$ reduction pathway via sequential $*NO_2 \rightarrow *NH_2 \rightarrow NH_3$ steps. For a comprehensive comparison, a pentagonal radar plot (Fig. 3e) summarizes five key performance descriptors: NH_3 YR, FE, current density, NO_2^- YR, and active site density. Cu_2/try-FeO_x outperforms the benchmark catalysts across all metrics, particularly those related to NH_3 production, confirming its superior electrocatalytic capability for NO_3^--to-NH_3 conversion.

Furthermore, NH_3 quantification was rigorously cross-validated using multiple methods to ensure accuracy and eliminate potential errors during the NO_3RR process. Besides the standard indophenol colorimetric test, ^{1}H NMR spectroscopy was directed using D_2O as the solvent to confirm the formation of $^{14}NH_4^+$. A well-resolved triplet signal observed between 6.6 and 7.2 ppm (Fig. S23), corresponding to the nuclear spin of ^{14}N (I=1), provides direct molecular evidence of NH_4^+ production via the reduction of $^{14}NO_3^-$. The NH_3 YR determined via NMR was 0.31 mmol h^{-1} cm^{-2} for Cu_2/try-FeO_x at −0.2 V vs. RHE, which closely matches the value obtained from the colorimetric method (Fig.s 3f and S24), thereby confirming the reliability of the indophenol blue method. Control experiments conducted without NO_3^- (Fig. S25) showed negligible NH_3 formation, ruling out contributions from background nitrogenous contaminants or ambient nitrogen fixation pathways. The long-term stability of Cu_2/try-FeO_x was evaluated through a 10-cycle chronoamperometric durability test (Fig. 3g). Although current density gradually decreased over successive cycles, full recovery occurred upon electrolyte replenishment, suggesting that the performance drop resulted from NO_3^- depletion rather than catalyst degradation. Moreover, the current density in NO_3RR is pH-dependent, and the electrolyte pH can vary due to the formation and consumption of reaction intermediates during the reaction. To assess this effect, the bulk pH of the electrolyte (1.0 M KOH+0.1 M KNO_3) was measured before and after a 10 h long-term NO_3RR test conducted at −0.2 V vs. RHE. The pH remained essentially unchanged (initial pH ~ 13.94; final pH ~ 14.01), confirming the high buffering capacity of the alkaline medium and ensuring a stable reaction environment throughout the NO_3RR process. UV–vis analysis of the catholyte (Fig. S26) showed that the NH_3 YR remained consistent across 10 repeated cycles (0.25–0.31 mmol h^{-1} cm^{-2}), with FE exhibiting only minimal variation, confirming the robust structural and electrochemical stability of the Cu_2/try-FeO_x catalyst. Post-electrolysis FESEM–EDS analysis (Fig. S27) confirmed that the Cu atoms remained atomically dispersed with no signs of aggregation or leaching, maintaining an oxidation state within the +1/+2 range, which supports redox cycling during NO_3^- activation and intermediate stabilization. Moreover, XPS, XRD, and Raman spectra (Fig.s S28–**S30**) revealed partial in situ phase transformation from α-Fe_2O_3 to Fe_3O_4, attributed to lattice oxygen reconfiguration under the reducing cathodic environment. Furthermore, the chemical stability of Cu under the applied potential was evaluated by ICP–OES analysis of the electrolyte after a 10 h NO_3RR durability test conducted at −0.2 V vs. RHE. The Cu concentration in the electrolyte was below 0.4 ppb, indicating negligible Cu leaching and excellent retention of Cu species in the Cu_2/try-FeO_x catalyst during prolonged electrolysis. This structural adjustment did not compromise catalytic performance, indicating the intrinsic durability of the Cu_2/try-FeO_x system. To benchmark the performance of the Cu_2/try-FeO_x catalyst, a comparative plot (Fig. 3h) illustrates the NH_3 YRs of leading top-performing NO_3RR catalysts reported in the literature. In addition to Fig. 3h, a comprehensive performance benchmarking summary—including electrolyte composition, NO_3^- concentration, and the applied potential corresponding to the data in Fig. 3h is provided in Table S4. The Cu_2/try-FeO_x catalyst achieved a record-high YR of 0.29 mmol h^{-1} cm^{-2}, surpassing state-of-the-art Cu-based systems. This highlights that integrating dual Cu atomic sites within an FeO_x matrix effectively combines the electronic advantages of Cu-DA catalysis with the redox flexibility of mixed-valence Fe oxides, offering a synergistic and robust alternative to noble metal–based NO_3RR systems.

2.4. *In situ and ex situ spectroelectrochemical probing of the NO_3RR mechanism*

To elucidate the NO_3RR pathway on the Cu_2/try-FeO_x catalyst, we employed in situ Raman spectroscopy and ex situ FTIR measurements. As shown in Fig. 4a and b, the in situ Raman spectroelectrochemical experimental setup and the resulting Raman spectra obtained under different applied cathodic potentials (−0.1 to −0.4 V vs. RHE) reveal the evolution of key vibrational features corresponding to the surface-bound intermediates. First, typical peaks at ~225 and ~670 cm^{-1}, corresponding to the A_{1g} lattice vibrations of α-Fe_2O_3 and Fe_3O_4, respectively, confirm the coexistence of the dual-phase iron oxides. With increasing negative potential, new Raman bands appear at ~1330 and ~1048 cm^{-1}, attributed to $*NO_2^-$ and $*NH_2$ intermediates, respectively [30–32]. These features indicate progressive NO_3^- reduction and stepwise hydrogenation occurring on the catalyst surface. The corresponding 3D Raman contour map (Fig. 4c) further visualizes the formation and transformation of these intermediates, demonstrating the catalyst's ability to stabilize $*NO_2^-$ and NH_x species. In addition, the ex situ FTIR spectra (Fig. 4d and e) of the catholyte after 1 h of electrolysis using Cu_2/try-FeO_x at different potentials confirm vibrational features of soluble nitrate-derived intermediates. Peaks at ~1350–1385 and 1230–1250 cm^{-1} resemble to the asymmetric stretching modes of NO_3^- and NO_2^-, respectively, while those at ~3300–3400 and ~1600 cm^{-1} are accredited to the N–H stretching and bending vibrations of the $*NH_2$ or NH_3 species [63–65]. The consistent presence and potential-dependent intensity changes of these bands confirm the stepwise reduction of NO_3^- via nitrogenous intermediates, with no detectable N_2O- or N_2-related vibrational features, confirming high selectivity toward NH_3 formation. In situ Raman and ex situ FTIR analyses under applied potential reveal a clear sequential NO_3^- transformation pathway: $NO_3^- \rightarrow NO_2^- \rightarrow *NH_2 \rightarrow NH_3$, consistent with an $8e^-/9H^+$ coupled electron transfer process (Fig. 4f) [66,67]. Notably, the agreement in intermediate identity and their potential-dependent evolution observed in situ Raman and ex situ FTIR findings strongly supports a concerted mechanism facilitated by the synergistic interplay between Cu-DA sites and the redox-active FeO_x heterostructure.

2.5. *Theoretical insights into the Cu-DA and NO_3RR reactant interactions*

To elucidate the enhanced catalytic performance of Cu_2/try-FeO_x in the NO_3RR, we performed DFT calculations on pristine FeO_x and Cu_2/try-FeO_x catalysts. As illustrated in Fig. 5a, two Cu atoms are asymmetrically immobilized on the L-tryptophan-functionalized FeO_X surface (Fig. S31), coordinated with lattice oxygen and amine groups. This configuration is thermodynamically stable, confirmed by cohesive energy and electron localization function analyses (Fig. S32). The strong Cu–O and Cu–N interactions stabilize the dual Cu configuration and enable efficient electronic coupling between Cu-DA and the FeO_x substrate. The charge density difference plot (Fig. 5b) reveals substantial interfacial charge redistribution at the Cu_2/try-FeO_x, with electron accumulation at the Cu sites (yellow regions) and partial depletion in the surrounding FeO_x matrix (blue regions), indicating electron transfer from FeO_x to Cu. This generates a locally electron-rich Cu environment that facilitates electrophilic NO_3^- adsorption and activation during the NO_3RR process. The PDOS analysis (Fig. 5c) shows an upward shift of the Cu *d*-band center toward the Fermi level compared with pristine FeO_X, implying enhanced orbital overlap with adsorbates. This shift promotes charge transfer and improves the overall electrocatalytic activity of the Cu_2/try-FeO_x catalyst.

Furthermore, we investigated the adsorption energy of NO_3^- on the Cu_2/try-FeO_x catalyst. Among the various configurations analyzed, configuration I (Fig. 5d) exhibited the most favorable chemisorption

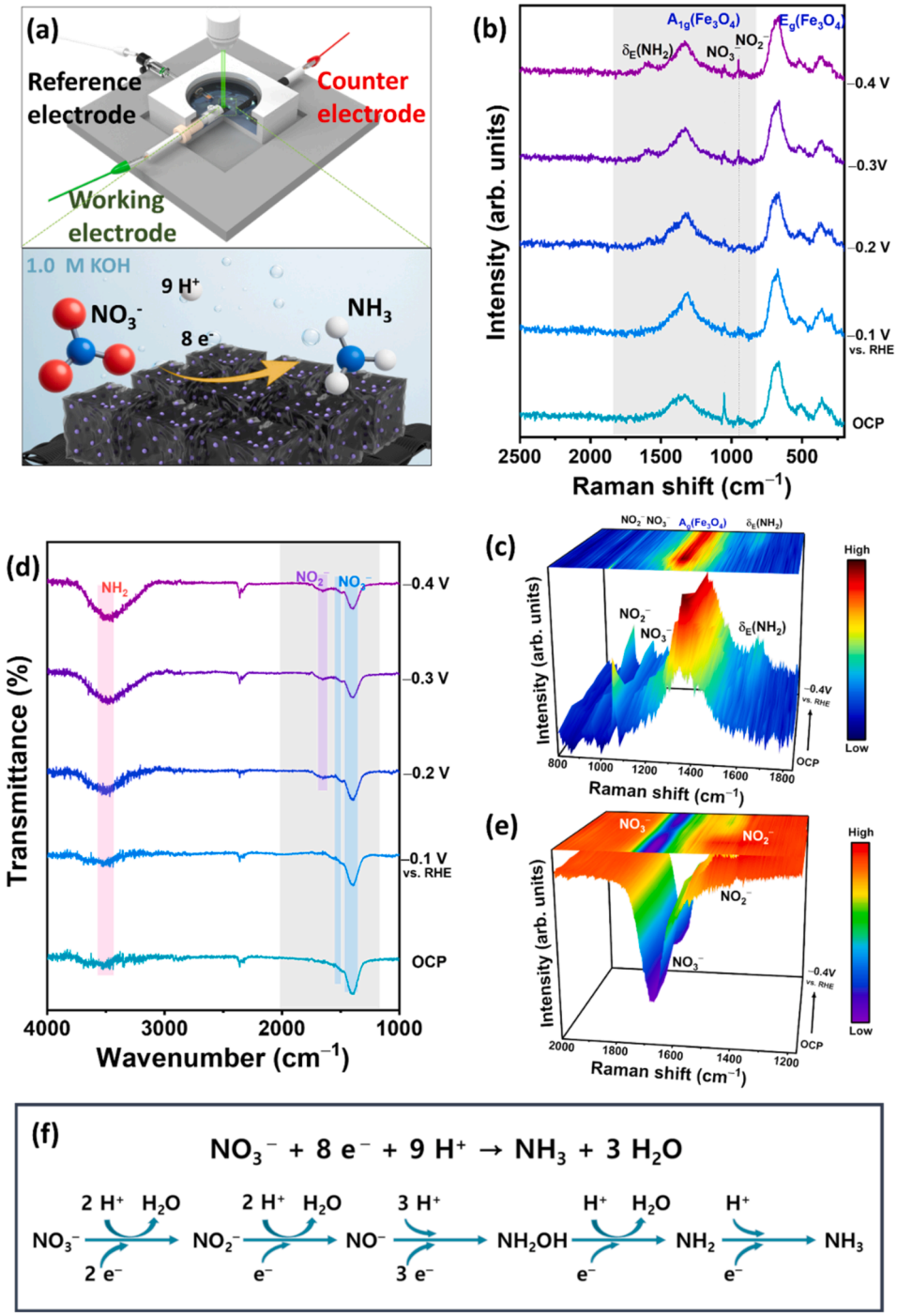

Fig. 4. (a–c) In situ Raman spectroelectrochemical experimental setup, Raman spectra recorded during the NO_3RR process on Cu_2/try-FeO_x at different reduction potentials, and their corresponding contour plots. (d,e) Ex situ FTIR spectra of the catholyte collected after 1 h of the NO_3RR using Cu_2/try-FeO_x at different reduction potentials and their corresponding contour plots. (f) Proposed NO_3RR mechanistic pathway.

energy of −2.13 eV, indicating strong thermodynamic affinity of NO_3^- at the Cu_2 active interface. By contrast, NO_3^- adsorption at other sites shown in configurations II, III, and IV (Fig. S33) exhibited significantly lower binding energies (−0.57, −1.15, and −0.29 eV, respectively), suggesting that the try-FeO_x substrate primarily facilitates charge transfer to the Cu centers rather than serving as the main adsorption site during the NO_3RR. For comparison, the binding energy of NO_3^- on pristine FeO_x was −1.34 eV (Fig. S34), which is weaker than that on the Cu_2/try-FeO_x, further confirming the enhanced adsorption capability resulting from Cu incorporation. The strong Cu–O interaction is further illustrated by the orbital interaction schematic (Fig. 5f), where backdonation from Cu *d*-orbitals to the *π antibonding orbital of NO_3^- occurs, while lone pairs from the oxygen atoms donate electron density into vacant Cu *d** orbitals. This classic donation–backdonation mechanism resembles ligand-field stabilization in organometallic complexes and contributes to the weakening of the N–O bonds in adsorbed NO_3^- species, thereby facilitating the continuous NO_3RR.

Based on the detected reaction intermediates from in situ and ex situ spectroelectrochemical analyses, a complete reaction pathway for NO_3^- to NH_3 on Cu_2/try-FeO_x and FeO_x is presented in Fig.s 5g and S35. The NO_3RR proceeds via a sequential hydrogenation–deoxygenation mechanism, as illustrated in Fig.s 5h and 5i, following the pathway: $*NO_3$ →

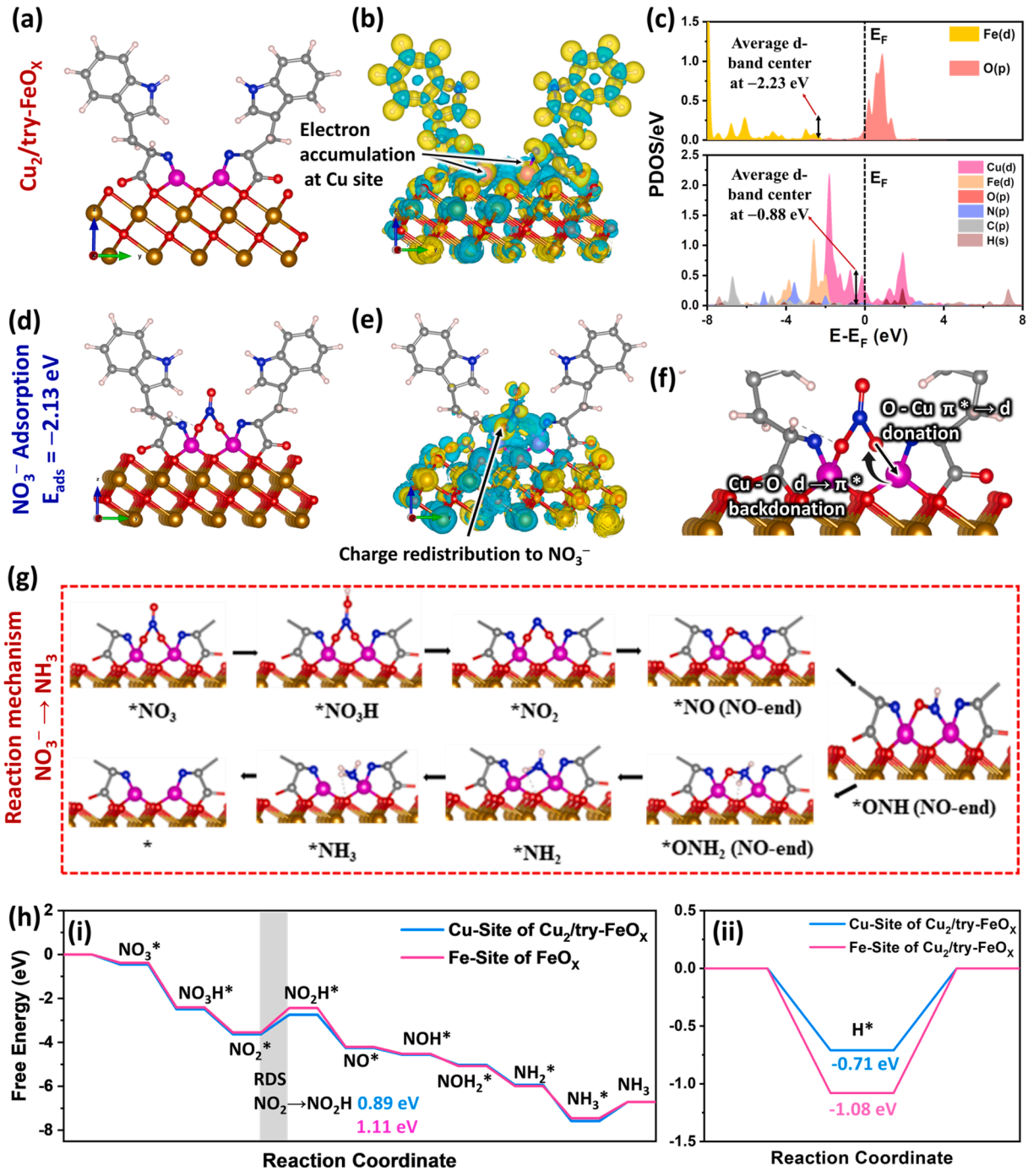

Fig. 5. (a) Optimized structure of Cu_2/try-FeO_x surface. (b) Charge density difference plot showing electron accumulation at the Cu site. (c) PDOS of FeO_x and Cu_2/try-FeO_x. (d) Optimized NO_3^- adsorption configuration on Cu_2/try-FeO_x. (e) Charge redistribution of Cu_2/try-FeO_x upon NO_3^- adsorption. (f) Schematic illustration of π-donation and backdonation between Cu *d*-orbitals and NO_3^-. (g) Reaction pathway for NO_3^- electroreduction to NH_3 with key adsorbed intermediates. (h-i) Gibbs free energy diagram for NO_3^- to NH_3 on Cu_2/try-FeO_x and FeO_x surfaces. (h-ii) *H adsorption on Cu_2/try-FeO_x surface.

$*NO_3H \rightarrow *NO_2 \rightarrow *NO_2H \rightarrow *NO \rightarrow *NOH \rightarrow *NOH_2 \rightarrow *NH_2 \rightarrow *NH_3 \rightarrow NH_3$ (desorption of NH_3 from the catalyst surface) [68–71]. Detailed reaction energies, zero-point energy corrections, and entropy contributions employed in the free-energy calculations are summarized in Table S5. Among these steps, the hydrogenation of $*NO_2$ to $*NO_2H$ is identified as the RDS, with a calculated energy barrier of 0.89 eV on Cu_2/try-FeO_x. Notably, this is significantly lower than the corresponding barrier of 1.11 eV on FeO_x, indicating that Cu incorporation effectively reduces the overpotential for the NO_3RR and improves the Cu_2/try-FeO_x catalytic efficiency. These results highlight the kinetic advantage of Cu_2/try-FeO_x in facilitating N–O bond dissociation, a crucial step in the NO_3RR catalysis. Site-specific free energy analyses (Fig. S36) reveal that the initial $NO_3^- \rightarrow *NO_3$ adsorption step is more thermodynamically favorable at the Cu sites (−0.65 eV) than the Fe sites (−0.51 eV), confirming enhanced reactant activation at Cu centers. Moreover, the energy barrier for the RDS at the Cu site is only 0.48 eV, signifying an efficient hydrogenation process during NO_3RR. For final product desorption, NH_3 exhibits a desorption energy of −0.66 eV from the Cu site, which is significantly more favorable than −1.02 eV from the Fe site. This moderate binding strength aligns with the Sabatier principle,

balancing adsorption and desorption to prevent catalyst poisoning while ensuring effective product release. In addition, during hydrogenation, active hydrogen species (*H) generated via water dissociation under alkaline conditions on the catalyst surface play a crucial role in promoting PCET processes [72]. To explore the hydrogen evolution dynamics, we examined *H adsorption on Cu and Fe sites within Cu_2/try-FeO_x (Fig.s 5h-ii and **S37**). The Fe site demonstrates strong *H adsorption (−1.08 eV), indicating its role as a primary *H generation site. By contrast, the Cu sites exhibit weaker *H adsorption (−0.71 eV), favoring hydrogen transfer rather than retention. This disparity in hydrogen binding strength suggests a synergistic dual-site hydrogenation mechanism, in which Fe sites function as transient *H reservoirs that facilitate proton activation and stabilization, followed by hydrogen spillover to adjacent Cu-DA sites. At the Cu centers, the transferred H participates in the selective hydrogenation of nitrogen-containing intermediates, thereby accelerating key NO_3RR steps while simultaneously suppressing the competing HER. Together, this cooperative interaction between the Cu and Fe centers enhances the kinetics and selectivity of the NO_3RR, promoting efficient N–O bond cleavage and NH_3 formation. The electronic and structural complementarity of the Cu-DA configuration thus underlies the superior catalytic performance of the Cu_2/try-FeO_x system [73,74].

2.6. *Zn–NO_3^- battery: integrated power generation and ammonia production*

The dual-functional Zn–NO_3^- battery system integrates energy conversion with chemical production, offering a promising approach for sustainable, decentralized NH_3 synthesis. As illustrated in Fig. 6a, the Zn-NO_3^- system uses a Zn metal anode immersed in 6.0 M KOH containing 0.1 M $Zn(OAc)_2$ and a cathodic compartment containing the Cu_2/try-FeO_x catalyst in 1.0 M KOH with 0.5 M KNO_3. The two chambers are divided by a Nafion membrane, enabling a spontaneous redox-coupled reaction. During discharge, the Zn plate undergoes oxidation at the anode, releasing electrons and generating chemical energy. This energy is directly used at the cathode to drive the NO_3RR to NH_3, removing the need for an external power supply. Thus, the device enables spontaneous chemical-to-electrical energy chemical energy conversion through internal redox coupling. The overall reaction mechanism during discharge is as follows:

$$Anode: 4Zn \rightarrow 4Zn^{2+} + 8e^-, \quad (1)$$

$$Cathode: NO_3^- + 6H_2O + 8e^- \rightarrow NH_3 + 9OH^-, \quad (2)$$

and

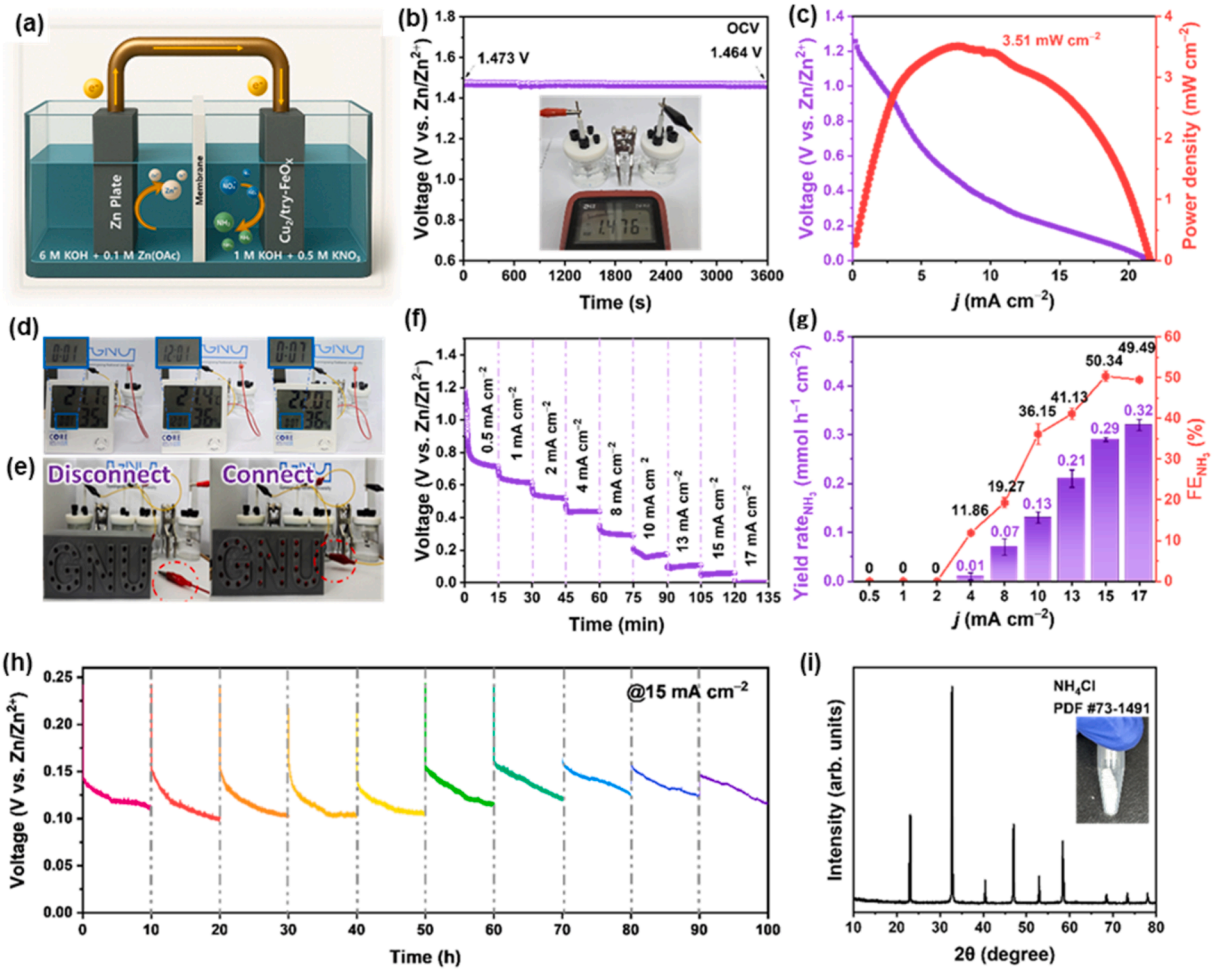

Fig. 6. (a) Graphic depiction of the Zn–NO_3^- battery assembly using Cu_2/try-FeO_x as the cathode. (b) OCV plot with inset showing the OCV value recorded on a multimeter for the Zn–NO_3^- battery assembled using the Cu_2/try-FeO_x cathode. (c) Discharge polarization and power density curves of the assembled Zn–NO_3^- battery. (d) Photograph of an electronic timer powered by the assembled Zn–NO_3^- battery with Cu_2/try-FeO_x cathode for 24 h. (e) Digital photographs of a 'GNU' pattern of 29 parallel red LEDs powered by the battery. (f) Discharge rate capability test at various current densities. (g) The difference in the NH_3 YR and FE with current densities. (h) Long-term discharge curves at 15 mA·cm^{-2} over 100 h. (i) XRD pattern of NH_4Cl powder recovered using acid trap after 15 h of electrolysis.

$$\text{Overall}: 4Zn + NO_3^- + 2H_2O \rightarrow 4Zn^{2+} + NH_3 + 9OH^-. \quad (3)$$

Electrochemical measurements of the Zn–NO_3^- battery were conducted using a two-chamber H-cell setup, as illustrated in Fig. S38. The OCV of the Zn–NO_3^- battery reaches ~1.24 V (Fig. 6b, inset with multimeter reading), which is sufficient to drive the NO_3RR at the Cu_2/try-FeO_x cathode. The discharge curve (Fig. 6c) shows a maximum power density of 3.61 mW cm^{-2}, demonstrating the battery's capability to deliver high voltage and moderate power density under ambient conditions. These findings highlight the practical feasibility of the Zn-NO_3^- battery to power electronic devices and directly drive the NO_3RR for NH_3 production via spontaneous electrochemical processes. As shown in Fig. 6d, a single battery system successfully powered a commercial clock for over 24 h under ambient conditions, highlighting excellent operational durability. Furthermore, connecting two Zn-NO_3^- batteries in series (Fig. 6e) confirmed the system's reversibility: upon disconnection, the clock ceased operation and resumed immediately upon reconnection. This on–off behavior verifies that the spontaneous electrocatalytic activity is driven solely by internal redox reactions without external bias. The rate performance of the Zn-NO_3^- battery was assessed through stepwise discharge at various current densities (Fig. 6f). The stable voltage output across different current conditions indicates excellent electrochemical stability and efficient mass transport kinetics at the Cu_2/try-FeO_x cathode under dynamic operating conditions. Quantitative analysis reveals an NH_3 YR of up to 0.29 mmol h^{-1} cm^{-2} with a maximum FE of 50.34% (Fig.s 6g and S39), confirming efficient electron utilization and selective NH_3 production with minimal competing side reactions. Durability testing further confirms the long-term performance of Cu_2/try-FeO_x cathode in Zn-NO_3^- battery application. As shown in Fig. 6h, galvanostatic discharge cycling over 100 h exhibits negligible voltage degradation, indicating the structural and catalytic robustness of the Cu_2/try-FeO_x electrode. To demonstrate its practical applicability, the electrosynthesized NH_3 was captured and converted into NH_4Cl powder via acid trapping (Fig. S40). The XRD pattern of the recovered solid (Fig. 6i) shows characteristic diffraction peaks matching standard NH_4Cl, confirming the successful transformation of NH_3 into a value-added product. Together, the high NH_3 YR, substantial FE, and stable power output validate the Zn–NO_3^- battery as a viable, energy-autonomous system for the NO_3RR. This dual-functional system offers a promising paradigm for integrating primary battery technology with decentralized electrosynthesis, particularly for sustainable NH_3 production.

3. Conclusions

Herein, we present a rationally designed Cu-DA catalyst (Cu_2/try-FeO_x), composed of asymmetrically coordinated Cu atomic pairs anchored on a CO_2 laser–engineered, L-tryptophan-functionalized mixed-phase Fe_3O_4/α-Fe_2O_3 heterostructure, enabling highly selective $8e^-/9H^+$ NO_3^- electroreduction to NH_3 under ambient environments. The catalyst achieves an NH_3 YR of 0.29 mmol h^{-1} cm^{-2} and a maximum FE of 88.5% at −0.2 V vs. RHE. When integrated into a Zn–NO_3^- battery, the system enables sustained, self-powered NO_3^- to NH_3 conversion for over 100 h. The spatially separated, asymmetrically coordinated Cu–N/O dual sites exhibit synergistic electronic interactions that facilitate efficient *H generation, NO_3^- activation, and intermediate hydrogenation. Combined in situ Raman spectroscopy, ex situ FTIR analysis, and DFT calculations corroborate a sequential reaction pathway of $*NO_3 \rightarrow *NO_2 \rightarrow *NO \rightarrow *NHO \rightarrow *NH_2O \rightarrow *NH_3 \rightarrow NH_3$, accompanied by effective suppression of competing byproducts (H_2/N_2/N_2O). This study highlights the role of DA site engineering and biofunctional support design in achieving selective and energy-efficient NO_3^- conversion, offering a versatile platform for decentralized and sustainable NH_3 production.

4. Experimental section

4.1. Synthesis of Fe-based Prussian blue analogues

The Fe-based Prussian blue analogue (FePBA) precursor was synthesized via a self-assembly co-precipitation process. Specifically, **Solution A** was obtained by dissolving 35 mM of $C_6H_5Na_3O_7$ and 12.25 mM of $FeCl_2{\cdot}4H_2O$ in 40 mL of DI water. Simultaneously, **Solution B** was prepared by dissolving 14 mM of $K_3[Fe(CN)_6]$ in 20 mL of DI tewater. **Solution B** was then added dropwise to **Solution A**n under continuous magnetic stirring at ambient temperature. The resulting mixture was stirred at 60 °C for 12 h. After, the precipitate was collected by centrifugation at 8000 rpm for 10 min, and washed thrice with DI water and ethanol to remove any unreacted species. The attained solid was dried in a vacuum oven at 60 °C for 3 h, yielding a pale brown powder referred to as FePBA.

4.2. Synthesis of Fe_3O_4/α-Fe_2O_3 cubic heterostructures

The as-synthesized FePBA powder was transferred into a ceramic crucible and kept in an air furnace. The sample was heated in air to 350 °C at heating rate of 5 °C min^{-1} and continued at this temperature for 1 h. After, the furnace was allowed to cool naturally. The resulting black powder was designated as Fe_3O_4/α-Fe_2O_3 **(**FeO_x) and stored in a desiccator for further use.

4.3. Surface functionalization of FeO_X with L-tryptophan

To prepare the L-tryptophan functionalized FeO_x (try-FeO_x), 5 mg of the prepared FeO_x and 2 mg of L-tryptophan were dispersed in 10 mL of ethanol in a 20 mL quartz vial. The mixture was subjected to ultrasonication for 10 min to ensure uniform dispersion. During sonication, the suspension was irradiated with a CO_2 laser (λ=10.6 μm, power=25 W) for 10 min. After irradiation, the suspension was centrifuged at 9000 rpm for 10 min, and the resulting product was washed three times with DI water and ethanol. The final product, try-FeO_x, was dried under vacuum at room temperature and stored in an airtight container.

4.4. Synthesis of Cu-DA on try-FeO_x

To synthesize Cu-DA anchored try-FeO_x (Cu_2/try-FeO_x), 1 mg of try-FeO_x was dispersed in 5 mL of ethanol containing 1 mM $Cu(NO_3)_2{\cdot}6H_2O$ in a quartz vial. The suspension was ultrasonicated for 5 min to ensure homogenous dispersion and to promote coordination between Cu^{2+} ions and surface functional groups. Simultaneously, the mixture was irradiated with a CO_2 laser (λ=10.6 μm, power=25 W) for 5 min during sonication. The resulting product was collected by centrifugation at 9000 rpm for 10 min, subsequently three washing cycles with ethanol and deionized water to remove any unbound ions or residual species. The final Cu_2/try-FeO_x catalyst was dried under vacuum and stored in an inert atmosphere (argon-filled glovebox) to prevent surface oxidation.

Detailed information regarding the synthesis procedure and experimental parameters is discussed in the Supporting Information.

CRediT authorship contribution statement

Yeryong Lee: Methodology, Investigation, Data curation. **Akash Prabhu Sundar Rajan:** Writing – original draft, Investigation, Formal analysis, Data curation. **Jayaraman Theerthagiri:** Writing – original draft, Validation, Formal analysis, Conceptualization. **Anuj Kumar:** Writing – review & editing, Software, Data curation. **Wanwisa Limphirat:** Visualization, Resources, Data curation. **Ahreum Min:** Writing –

review & editing, Validation, Investigation, Data curation. **Myong Yong Choi:** Writing – review & editing, Supervision, Project administration, Funding acquisition, Conceptualization.

Declaration of competing interest

The authors declare that they have no known competing financial interests or personal relationships that could have appeared to influence the work reported in this paper.

Acknowledgements

This research was supported by Korea Basic Science Institute (National research Facilities and Equipment Center) grant funded by the Ministry of Education (No. 2019R1A6C1010042, RS-2025-12872968, and RS-2024-00434932) and by the Korea government (MSIT) (PG2025039-02). The authors acknowledge financial support from the National Research Foundation of Korea (NRF) (2022R1A2C2010686, RS-2025-02634080, and RS-2024-00405324) and Core-Facility Center for Photochemistry & Nanomaterials, Gyeongsang National University, In-situ Cryo X-ray Absorption Spectrometer, IC-XAS (NFEC-2025-07-307201).

Appendix A. Supplementary data

Supplementary data to this article can be found online at https://doi.org/10.1016/j.apmate.2026.100407.

References

[1] I. Muzammil, Y.N. Kim, H. Kang, D.K. Dinh, S. Choi, C. Jung, Y.H. Song, E. Kim, J. M. Kim, D.H. Lee, Plasma catalyst-integrated system for ammonia production from H_2O and N_2 at atmospheric pressure, ACS Energy Lett. 6 (2021) 3004–3010.
[2] S.F. Jiang, Y. Tang, X.Y. Zheng, M. Zhao, Electrocatalytic synthesis of ammonia using transition metal-based catalysts under ambient conditions: a review, Environ. Chem. Lett. 23 (2025) 1247–1273.
[3] C. Smith, A.K. Hill, L. Torrente-Murciano, Current and future role of Haber–Bosch ammonia in a carbon-free energy landscape, Energy Environ. Sci. 13 (2020) 331–344.
[4] J. Kundu, T. Bhoyar, S. Park, H. Jin, K. Lee, S.I. Choi, Recent advances in single- and dual-atom catalysts for efficient nitrogen electro-reduction and their perspectives, Adv. Powder Mater. 4 (2025) 100279.
[5] H. Liang, A. Li, N. Yuan, Multifunctional metal–organic framework-based electrocatalysts: from CO_2 reduction and ammonia synthesis to urea production, Adv. Powder Mater. (2025) 100370.
[6] W. Gao, Z. Yan, S. Tian, J. Cui, B. Xie, Q. Jiao, C. Zhong, J. Liu, Modulate the strength of *H adsorption by changing the spin state over Cu/Co dual−active sites accelerating ammonia electrochemical synthesis kinetics, Appl. Catal. B Environ. Energy 377 (2025) 125495.
[7] W. Ye, Y. Yao, X. Wei, M. Xu, S. Zhao, W. Wang, G. Jia, F. Dai, P. Gao, X. Lu, Continuous intermediates spillover boosts electrochemical nitrate conversion to ammonia over dual single-atom alloy, Angew. Chem. Int. Ed. 64 (2025) e202509303.
[8] S.C. D'Angelo, A.J. Martín, S. Cobo, D.F. Ordóñez, G. Guillén-Gosálbez, J. Pérez-Ramírez, Environmental and economic potential of decentralised electrocatalytic ammonia synthesis powered by solar energy, Energy Environ. Sci. 16 (2023) 3314–3330.
[9] H. Zhang, K. Fang, J. Yang, H. Chen, J. Ning, H. Wang, Y. Hu, Strategies and applications of electrocatalytic nitrate reduction towards ammonia, Coord. Chem. Rev. 506 (2024) 215723.
[10] Y. Xiong, Y. Wang, J. Zhou, F. Liu, F. Hao, Z. Fan, Electrochemical nitrate reduction: ammonia synthesis and the beyond, Adv. Mater. 36 (2024) 2304021.
[11] W.D. Zhang, H. Dong, L. Zhou, H. Xu, H.R. Wang, X. Yan, Y. Jiang, J. Zhang, Z. G. Gu, Fe single-atom catalysts with pre-organized coordination structure for efficient electrochemical nitrate reduction to ammonia, Appl. Catal. B Environ. 317 (2022) 121750.
[12] K. Yang, S.H. Han, C. Cheng, C. Guo, T. Li, Y. Yu, Unveiling the reaction mechanism of nitrate reduction to ammonia over cobalt-based electrocatalysts, J. Am. Chem. Soc. 146 (2024) 12976–12983.
[13] X. Shi, M. Xie, K. Yang, Y. Niu, H. Ma, Y. Zhu, J. Li, T. Pan, X. Zhou, Y. Cui, Synergistic effect of Ni/$Ni(OH)_2$ core-shell catalyst boosts tandem nitrate reduction for ampere-level ammonia production, Angew. Chem. 136 (2024) e202406750.
[14] Y. Wang, M. Zheng, Y. Li, L. Zhu, H. Li, Q. Wang, H. Zhao, J. Zhang, Y. Dong, Y. Zhu, Atomically dispersed NiO_x cluster on high-index Pt facets boost ethanol electrooxidation through long-range synergistic sites, Adv. Powder Mater. 3 (2024) 100244.
[15] Y. Fu, S. Wang, Y. Wang, P. Wei, J. Shao, T. Liu, G. Wang, X. Bao, Enhancing electrochemical nitrate reduction to ammonia over Cu nanosheets via facet tandem catalysis, Angew. Chem. Int. Ed. 62 (2023) e202303327.
[16] K. Chen, D. Ma, Y. Zhang, F. Wang, X. Yang, X. Wang, H. Zhang, X. Liu, R. Bao, K. Chu, Urea electrosynthesis from nitrate and CO_2 on diatomic alloys, Adv. Mater. 36 (2024) 2402160.
[17] Z. Sun, R. Niu, S. Shang, Y. Guo, H. Zhang, X. Liu, L. Feng, K. Chu, Plasma-electrocatalytic synthesis of urea from air and CO_2, Nat. Commun. 16 (2025) 8837.
[18] Z. Sun, R. Niu, S. Shang, R. Liang, K. Chu, Electrochemical urea synthesis from CO_2 and NO on p-block Bi isolated sites via *CO-mediated C–N coupling, Nano Res. Energy 4 (2025) e9120198.
[19] T. Hou, T. Shan, H. Rong, J. Zhang, Nitrate electroreduction to ammonia over copper-based catalysts, ChemSusChem 18 (2025) e202402331.
[20] S. Chen, F. Farzinpour, N. Kornienko, Dynamic active sites behind Cu-based electrocatalysts: original or restructuring-induced catalytic activity, Chem 11 (2025) 102575.
[21] J.C. de Almeida, Y. Wang, T.A. Rodrigues, P.H. Nunes, V.R. de Mendonça, P. H. Falsetti, L.V. Savazi, T. He, A.V. Bardakova, A.V. Rudakova, Copper-based materials for photo and electrocatalytic process: advancing renewable energy and environmental applications, Adv. Funct. Mater. (2025) 2502901.
[22] Y. Li, Q. Lei, W.T. Hong, X. Liu, C. Xue, J.K. Kim, Transition metal-based materials for electrochemical and photoelectrochemical carbon-free nitrogen cycling as H-carrier, exploration, Exploration 5 (2025) 20240245.
[23] S. Tian, R. Wu, H. Liu, C. Yan, Z. Qi, P. Song, W.J. Chen, L. Song, Z. Wang, C. Lv, Realizing unconventional tandem nitrate reduction for efficient ammonia electrosynthesis enabled by Co, Fe dual-site conjugated metal organic frameworks, Angew. Chem. Int. Ed. 64 (2025) e202510665.
[24] X. Long, T. Zhong, F. Huang, P. Li, H. Zhao, J. Fang, D. Shu, C. He, Exploring microenvironmental configuration effects of Cu-based catalysts on nitrate electrocatalytic reduction selectivity, Appl. Catal. B Environ. Energy 365 (2025) 124944.
[25] X. Long, T. Li, Y. Wu, F. Huang, X. Guo, H. Zhao, S. Tian, D. Shu, C. He, Review of Cu-based dual-site catalysts for multi-step nitrate reduction: bridging material properties and catalytic mechanisms through strategic design, Small 21 (2025) 2502414.
[26] Z. Sun, H. Zhang, L. Cao, X. Liu, D. Wu, X. Shen, X. Zhang, Z. Chen, S. Ru, X. Zhu, Understanding synergistic catalysis on Cu–Se dual atom sites via operando x-ray absorption spectroscopy in oxygen reduction reaction, Angew. Chem. Int. Ed. 62 (2023) e202217719.
[27] B. Chen, D. Shi, R. Deng, X. Xu, W. Liu, Y. Wei, Z. Liu, S. Zhong, J. Huang, Y. Yu, Leveraging atomic-scale synergy for selective CO_2 electrocatalysis to CO over CuNi dual-atom catalysts, ACS Catal. 14 (2024) 16224–16233.
[28] C. Chen, Z. Sun, G. Qin, B. Wang, M. Liu, Q. Liang, X. Li, R. Pang, Y. Guo, Y. Li, Asymmetrically coordinated Cu dual-atom-sites enables selective CO_2 electroreduction to ethanol, Adv. Mater. 36 (2024) 2409797.
[29] S. Li, A. Guan, C. Yang, C. Peng, X. Lv, Y. Ji, Y. Quan, Q. Wang, L. Zhang, G. Zheng, Dual-atomic Cu sites for electrocatalytic CO reduction to C2+ products, ACS Mater. Lett. 3 (2021) 1729–1737.
[30] Z. Lian, D. Luo, J. Yang, Y. Yang, S. Tang, H. Li, D. Zhang, H. Li, Spatial decoupling of adsorption and transformation sites on ag-cu dual-single-atom catalysts for highly selective photocatalytic nitrate-to-ammonia reduction, Angew. Chem. Int. Ed. 65 (2025) e202516964.
[31] X. Su, M. Li, Y. Wen, F. Sun, B. Shan, Atomically paired Cu–Co dual sites for near-unity ammonia selectivity in nitrate electroreduction, J. Am. Chem. Soc. 147 (2025) 46471–46482.
[32] A.P.S. Rajan, J. Theerthagiri, P. Junmon, W. Limphirat, N. Yodsin, M.Y. Choi, Atomic precision CoCu heterodimers with pseudo-D3h symmetry enable tandem nitrate reduction, Adv. Sci. (2025) e23909.
[33] K. Huang, K. Tang, M. Wang, Y. Wang, T. Jiang, M. Wu, Boosting nitrate to ammonia via the optimization of key intermediate processes by low-coordinated Cu–Cu sites, Adv. Funct. Mater. 34 (2024) 2315324.
[34] Y. Wang, Q. Li, Y. Li, B. Xu, J. Yang, Gram-scale ammonia synthesis via electrochemical nitrate reduction using enzyme-inspired dual-atomic Cu catalyst, Angew. Chem. 64 (2025) e202510139.
[35] Y. Wang, C. Tang, Q. Li, T. Xiao, F. Xiong, Theoretical prediction of efficient Cu-based dual-atom alloy catalysts for electrocatalytic nitrate reduction to ammonia via high-throughput first-principles calculations, J. Mater. Chem. A 13 (2025) 3765–3776.
[36] C. Feng, M.B. Faheem, J. Fu, Y. Xiao, C. Li, Y. Li, Fe-based electrocatalysts for oxygen evolution reaction: progress and perspectives, ACS Catal. 10 (2020) 4019–4047.
[37] W. Chen, S. Yang, H. Liu, F. Huang, Q. Shao, L. Liu, J. Sun, C. Sun, D. Chen, L. Dong, Single-atom Ce-modified α-Fe_2O_3 for selective catalytic reduction of NO with NH_3, Environ. Sci. Technol. 56 (2022) 10442–10453.
[38] W. Li, C. Liu, C. Gu, J.H. Choi, S. Wang, J. Jiang, Interlayer charge transfer regulates single-atom catalytic activity on electride/graphene 2D heterojunctions, J. Am. Chem. Soc. 145 (2023) 4774–4783.
[39] J. Liu, X. Yang, F. Si, B. Zhao, X. Xi, L. Wang, J. Zhang, X.Z. Fu, J.L. Luo, Interfacial component coupling effects towards precise heterostructure design for efficient electrocatalytic water splitting, Nano Energy 103 (2022) 107753.

[40] J. Hu, A. Al-Salihy, J. Wang, X. Li, Y. Fu, Z. Li, X. Han, B. Song, P. Xu, Improved interface charge transfer and redistribution in CuO-CoOOH p-n heterojunction nanoarray electrocatalyst for enhanced oxygen evolution reaction, Adv. Sci. 8 (2021) 2103314.
[41] J. Park, J. Theerthagiri, N. Yodsin, W. Limphirat, P. Junmon, M.Y. Choi, CO_2 laser-stabilized Ni–Co dual single-atomic sites for energy generation and ammonia harvesting, Adv. Mater. 37 (2025) 2506137.
[42] X. Zhao, W.P. Li, Y. Cao, A. Portniagin, B. Tang, S. Wang, Q. Liu, D.Y. Yu, X. Zhong, X. Zheng, Dual-atom Co/Ni electrocatalyst anchored at the surface-modified $Ti_3C_2T_x$ MXene enables efficient hydrogen and oxygen evolution reactions, ACS Nano 18 (2024) 4256–4268.
[43] X. Yang, W. Song, K. Liao, X. Wang, X. Wang, J. Zhang, H. Wang, Y. Chen, N. Yan, X. Han, Cohesive energy discrepancy drives the fabrication of multimetallic atomically dispersed materials for hydrogen evolution reaction, Nat. Commun. 15 (2024) 8216.
[44] Y. Chen, Y. Yao, W. Zhao, L. Wang, H. Li, J. Zhang, B. Wang, Y. Jia, R. Zhang, Y. Yu, Precise solid-phase synthesis of CoFe@FeO_x nanoparticles for efficient polysulfide regulation in lithium/sodium-sulfur batteries, Nat. Commun. 14 (2023) 7487.
[45] Z. Xue, L. Li, L. Cao, W. Zheng, W. Yang, X. Yu, A simple method to fabricate $NiFe_2O_4$/NiO@Fe_2O_3 core-shelled nanocubes based on Prussian blue analogues for lithium ion battery, J. Alloys Compd. 825 (2020) 153966.
[46] X. Yang, B. Jin, L. Yu, F. Zhu, Y. Xu, R. Liu, Preparation and characterization of magnetic α-Fe_2O_3/Fe_3O_4 heteroplasmon nanorods via the ethanol solution combustion process of ferric nitrate, Mater. Res. Express 8 (2021) 025011.
[47] B. Lei, D. Xu, B. Wei, T. Xie, C. Xiao, W. Jin, L. Xu, In situ synthesis of α-Fe_2O_3/Fe_3O_4 heterojunction photoanode via fast flame annealing for enhanced charge separation and water oxidation, ACS Appl. Mater. Interfaces 13 (2021) 4785–4795.
[48] M.S. Saeed, J. Seyed-Yazdi, H. Hekmatara, Fe_2O_3/Fe_3O_4/PANI/MWCNT nanocomposite with the optimum amount and uniform orientation of Fe_2O_3/Fe_3O_4 NPs in polyaniline for high microwave absorbing performance, J. Alloys Compd. 843 (2020) 156052.
[49] J. Lian, X. Duan, J. Ma, P. Peng, T. Kim, W. Zheng, Hematite (α-Fe_2O_3) with various morphologies: ionic liquid-assisted synthesis, formation mechanism, and properties, ACS Nano 3 (2009) 3749–3761.
[50] X. Huang, J. Zhu, B. Ge, K. Deng, X. Wu, T. Xiao, T. Jiang, Z. Quan, Y.C. Cao, Z. Wang, Understanding Fe_3O_4 nanocube assembly with reconstruction of a consistent superlattice phase diagram, J. Am. Chem. Soc. 141 (2019) 3198–3206.
[51] M. Liu, J.A. Wang, W. Klysubun, G.G. Wang, S. Sattayaporn, F. Li, Y.W. Cai, F. Zhang, J. Yu, Y. Yang, Interfacial electronic structure engineering on molybdenum sulfide for robust dual-pH hydrogen evolution, Nat. Commun. 12 (2021) 5260.
[52] Y. Zhou, P. Guan, F. Chen, Z. Feng, H. Jia, T. Liang, M. Li, T. Wan, R. Tian, Z. Han, Engineering work functions of cobalt-doped manganese oxide based electrocatalysts for highly efficient oxygen evolution reaction, J. Colloid Interface Sci. 642 (2023) 23–28.
[53] Guillermo Tostado-Blazquez, Saptami Suresh Shetty, Saravanan Yuvaraja, Jose L. Cerrillo, Veerappan Mani, K.N. Salama, One-step synthesis of copper single-atom nanozymes for electrochemical sensing applications, Small Sci. 4 (2024) 2300259.
[54] A.R. Safira, M. Kaseem, Interfacial and electronic modulation of M-bridged heterostructures with L-tryptophan and transition metallic oxides: enhancing corrosion resistance and photocatalytic activity, ACS Appl. Mater. Interfaces 15 (2023) 59806–59825.
[55] A. Mohtasebi, T. Chowdhury, L.H. Hsu, M.C. Biesinger, P. Kruse, Interfacial charge transfer between phenyl-capped aniline tetramer films and iron oxide surfaces, J. Phys. Chem. C 120 (2016) 29248–29263.
[56] S. Thoonen, K.L. Tuck, D.R. Turner, Discrete metallosupramolecular architectures with amino acids, Coord. Chem. Rev. 522 (2025) 216203.
[57] J. Ren, M. Das, H. Osthues, M. Nyenhuis, B. Schulze Lammers, E. Kolodzeiski, H. Mönig, S. Amirjalayer, H. Fuchs, N.L. Doltsinis, The electron-rich and nucleophilic N-heterocyclic imines on metal surfaces: binding modes and interfacial charge transfer, J. Am. Chem. Soc. 146 (2024) 7288–7294.
[58] K. Lee, J. Shim, H. Ji, J. Kim, H.S. Lee, H. Shin, M.S. Bootharaju, K.S. Lee, W. Ko, J. Lee, Tailoring cobalt spinel oxide with site-specific single atom incorporation for high-performance electrocatalysis, Energy Environ. Sci. 17 (2024) 3618–3628.
[59] Y. Zhu, Q. Zhang, Y. Zheng, G. Li, R. Gao, Z. Piao, D. Luo, R.H. Gao, M. Zhang, X. Xiao, Uncoordinated Chemistry Enables Highly Conductive and Stable electrolyte/filler Interfaces for solid-state lithium–sulfur Batteries, 120, Proceedings of the National Academy of Sciences, 2023 e2300197120.
[60] K. Ebner, A.H. Clark, V.A. Saveleva, G. Smolentsev, J. Chen, L. Ni, J. Li, A. Zitolo, F. Jaouen, U.I. Kramm, Time-resolved potential-induced changes in Fe/N/C-catalysts studied by in situ modulation excitation X-ray absorption spectroscopy, Adv. Energy Mater. 12 (2022) 2103699.
[61] C. Marini, A.M.D. Rovira, N. Ramanan, W. Olszewski, B. Joseph, L. Simonelli, Combined micro X-ray absorption and fluorescence spectroscopy to map phases of complex systems: the case of sphalerite, Sci. Rep. 9 (2019) 18857.
[62] J. Lan, Z. Wang, C.W. Kao, Y.R. Lu, F. Xie, Y. Tan, Isolating Cu-Zn active-sites in ordered intermetallics to enhance nitrite-to-ammonia electroreduction, Nat. Commun. 15 (2024) 10173.
[63] D.H. Lee, J. Theerthagiri, N. Yodsin, W. Limphirat, S. Jungsuttiwong, M.Y. Choi, Paradigm for swift dual single-atom stabilization on MBene using a CO_2 laser in trifecta energy with ammonia production, Appl. Catal. B Environ. Energy 385 (2026) 126246.
[64] S. Lee, J. Theerthagiri, S.H. Pan, J.C. Jiang, M.Y. Choi, Infrared-driven high-entropy perovskites for efficient nitrate-to-ammonia conversion via B-site engineering, Mater. Today 92 (2025) 44–60.
[65] M. Kasiviswanathan, J. Theerthagiri, A. Watwiangkham, A. Min, S. Jungsuttiwong, M.Y. Choi, Phase-stabilized core@shell $NiFe_2O_4$@$CoFe_2O_4$ nanocages for the integrated energy and electroreduction of nitrate-to-ammonia, Appl. Catal. B Environ. Energy 380 (2026) 125775.
[66] Y. Lee, J. Theerthagiri, N. Yodsin, A. Min, C.J. Moon, S. Jungsuttiwong, M.Y. Choi, Mitigating intraphase catalytic-domain transfer via CO_2 laser for enhanced nitrate-to-ammonia electroconversion and zn-nitrate battery behavior, Angew. Chem. Int. Ed. 63 (2024) e202413774.
[67] Akash Prabhu Sundar Rajan, Jayaraman Theerthagiri, Wanwisa Limphirat, Anuj Kumar, Raja Arumugam Senthil, M.Y. Choi, Pulsed laser-twisted spinel-to-rocksalt high-entropy 3d-metal oxides for selective ammonia electrosynthesis, Small 21 (2025) 2504457.
[68] T. Begildayeva, J. Theerthagiri, W. Limphirat, A. Min, S. Kheawhom, M.Y. Choi, Deciphering indirect nitrite reduction to ammonia in high-entropy electrocatalysts using in situ raman and x-ray absorption spectroscopies, Small 20 (2024) 2400538.
[69] Z. Li, M. Zheng, C. Yan, D. Yang, R. Yang, C. Zhang, H. Liu, P. Song, C. Yin, Z. Qi, Stabilizing Cu^0-$Cu^{\delta+}$ sites via ohmic contact interface engineering for ampere-level nitrate electroreduction to ammonia, Nat. Commun. 16 (2025) 8940.
[70] Z. Li, Z. Shi, Y. Ou, L. Zhong, C. Yan, C. Zhang, K. Song, H. Liu, D. Liu, P. Song, Pulsed electrocatalysis driven efficient ammonia synthesis by facilitating *NOOH formation and balancing *H supply, Angew. Chem. Int. Ed. 64 (2025) e202510287.
[71] Z. Xiang, Y.R. Lu, L. Meng, J. Lan, F. Xie, S. Gao, J. Li, M. Luo, M. Peng, Y. Tan, Active hydrogen enrichment on Cu_6Sn_5-type high entropy intermetallics for efficient nitrate reduction reaction, Adv. Mater. 37 (2025) 2501886.
[72] Y. Chen, H. Bai, J. Lan, C.W. Kao, F. Xie, L. Meng, J. Li, Y.R. Lu, M. Peng, H. Pan, Ru single atoms anchored in metal borides enable hydrogen spillover for superior electrochemical ammonia production, Angew. Chem. Int. Ed. 64 (2025) e202504568.
[73] B. Zhou, L. Yu, W. Zhang, X. Liu, H. Zhang, J. Cheng, Z. Chen, H. Zhang, M. Li, Y. Shi, Cu_1−Fe dual sites for superior neutral ammonia electrosynthesis from nitrate, Angew. Chem. Int. Ed. 63 (2024) e202406046.
[74] Y. Hua, N. Song, Z. Wu, Y. Lan, H. Luo, Q. Song, J. Yang, Cu–Fe synergistic active sites boost kinetics of electrochemical nitrate reduction, Adv. Funct. Mater. 34 (2024) 2314461.

Akash Prabhu is a PhD student in the Department of Chemistry at Gyeongsang National University focusing on electrochemical small-molecule conversion. His research focuses on designing and understanding electrocatalysts for reactions involving nitrate, CO_2, and other energy-related molecules.

Dr. Jayaraman Theerthagiri is currently working as Research Professor in the Department of Chemistry, Gyeongsang National University, South Korea. Dr. Theerthagiri always expresses deep gratitude to his beloved children, Yokith and Ranika, for their unconditional love. He graduated from Sacred Heart College, Tirupattur (affiliated to Thiruvalluvar University, India) with a B.Sc, Chemistry degree in 2009. He received his M.Sc, Chemistry degree from Ramakrishna Mission Vivekananda College, Chennai (affiliated to University of Madras, India) in 2011, and his Ph.D. degree from Thiruvalluvar University in 2017 and later he worked as an Assistant Professor in the Center for Nanoscience and Nanotechnology, Sathyabama Institute of Science and Technology (Deemed to be University), Chennai, India from 2017 to 2019. His current research is focused on the development of electrocatalysts for the production of energy-saving fuel and value-added chemicals.

Ahreum Min is currently an Associate Professor in the Department of Chemistry at Gyeongsang National University (GNU), Jinju, South Korea. She received her Ph.D. in Physical Chemistry from GNU in 2016. She worked as a postdoctoral researcher in the Department of Chemistry at Chungbuk National University (South Korea) and at the University of Hawai'i at Manoa (USA). Her research focuses on photochemistry and the development of in-situ multimodal spectroscopic approaches for investigating reaction mechanisms in both gas-phase and condensed-phase systems.

Professor Myong Yong Choi is a distinguished physical chemist with expertise in spectroscopy, laser photochemistry, and nanomaterials. He is a senior faculty member in the Department of Chemistry at Gyeongsang National University (GNU), South Korea, where he also serves as the Director of the Core-Facility Center for Photochemistry and Nanomaterials and the Director of the Graduate School for Molecular Material Chemistry. Prof. Choi earned his M.S. in Chemistry from the University of Idaho and his Ph.D. from the University of North Carolina at Chapel Hill. He subsequently conducted post-doctoral research in the Faculty of Science at the University of Southern California. His research group has pioneered a variety of laser-assisted techniques for the synthesis and characterization of metal nanoparticles, alloys, nanocomposites, and coordination polymers. These efforts have significantly advanced applications in spectroscopy, chemical sensing, and catalysis. More recently, his team has expanded into the laser-mediated fabrication of functional nanomaterials and biomaterials aimed at energy conversion and environmental remediation. Prof. Choi has authored over 250 peer-reviewed publications in high-impact international journals, holds fifteen patents, and has contributed to two edited books and twelve book chapters. He has also been invited to deliver numerous plenary, keynote, and invited lectures at leading international conferences and research institutions. In addition to his research accomplishments, Prof. Choi has served on key administrative and advisory roles at GNU, including the Center for Laboratory Safety, the Center for Research Facilities, and as Chair of the Department of Chemistry. He has also contributed to scientific advisory boards of external institutions. His contributions to science and education have been recognized through multiple awards and honors, including the Commendation Award, KCS/Sigma-Aldrich Excellent Chemistry Award, the Ministry of Education's Top 50 Excellent Research Achievements, Lifetime Membership in the Gaechuck Hanlim Academy, the Gaechuck Award for Excellence in Teaching, the KCS Kim Myung Soo Award, the KCS Young Physical Chemist Award, and the Ministry of Environment's Top 50 Environmental Technology Award.